Strathprints Institutional Repository

Lockerby, Duncan A. and Duque Daza, C.A. and Borg, Matthew Karl and Reese, Jason (2013) *Time-step coupling for hybrid simulations of multiscale flows.* Journal of Computational Physics, 237. pp. 344-365. ISSN 0021-9991

Journal of Computational Physics 237 (2013) 344–365

Contents lists available at SciVerse ScienceDirect

Journal of Computational Physics

journal homepage: www.elsevier.com/locate/jcp

Time-step coupling for hybrid simulations of multiscale flows

Duncan A. Lockerby [a,*], Carlos A. Duque-Daza [a,b], Matthew K. Borg [c], Jason M. Reese [c]

[a] School of Engineering, University of Warwick, Coventry CV4 7AL, UK
[b] Department of Mechanical and Mechatronics Engineering, Universidad Nacional de Colombia, Bogota, Colombia
[c] Department of Mechanical and Aerospace Engineering, University of Strathclyde, Glasgow G1 1XJ, UK

ARTICLE INFO

Article history:
Received 14 August 2012
Received in revised form 12 November 2012
Accepted 14 November 2012
Available online 7 December 2012

Keywords:
Multiscale simulations
Unsteady micro/nano flows
Hybrid methods
Scale separation

ABSTRACT

A new method is presented for the exploitation of time-scale separation in hybrid continuum-molecular models of multiscale flows. Our method is a generalisation of existing approaches, and is evaluated in terms of computational efficiency and physical/numerical error. Comparison with existing schemes demonstrates comparable, or much improved, physical accuracy, at comparable, or far greater, efficiency (in terms of the number of time-step operations required to cover the same physical time). A leapfrog coupling is proposed between the 'macro' and 'micro' components of the hybrid model and demonstrates potential for improved numerical accuracy over a standard simultaneous approach. A general algorithm for a coupled time step is presented. Three test cases are considered where the degree of time-scale separation naturally varies during the course of the simulation. First, the step response of a second-order system composed of two linearly-coupled ODEs. Second, a micro-jet actuator combining a kinetic treatment in a small flow region where rarefaction is important with a simple ODE enforcing mass conservation in a much larger spatial region. Finally, the transient start-up flow of a journal bearing with a cylindrical rarefied gas layer. Our new time-stepping method consistently demonstrates as good as or better performance than existing schemes. This superior overall performance is due to an adaptability inherent in the method, which allows the most-desirable aspects of existing schemes to be applied only in the appropriate conditions.

1. Introduction

Advances in micro and nano technologies are presenting new challenges for engineering science. In fluid dynamics, the number of flow systems that need an appreciation of the multiscale physics involved is increasing substantially. Modelling such flows can require resolving microscopic processes in order to accurately predict macroscopic behaviour: micro- and millisecond effects are important in micro and nano flows, but depend on the outcome of pico-second molecular processes. This presents a formidable multiscale problem.

Any fluid flow can in principle be simulated by employing a suitable molecular or kinetic model over the entire flow domain. While this is practicable when studying the flows, for example, in a carbon nanotube, of a small group of proteins in solution, or other very small-scale systems, in engineering problems the simulation domain is often very much larger, making this approach computationally impractical. However, it is possible to identify regions in the space domain and periods in time where 'scale separation' exists; that is, where processes occurring on a small scale are only loosely coupled with the behaviour on a much larger scale. In such conditions, a macroscopic description of the flow on the larger scale can be adopted

---

[*] Corresponding author.
E-mail address: duncan.lockerby@warwick.ac.uk (D.A. Lockerby).

0021-9991/$ - see front matter © 2012 Elsevier Inc. All rights reserved.
http://dx.doi.org/10.1016/j.jcp.2012.11.032

(e.g. the continuum conservation laws) coupled to molecular or gas-kinetic simulations covering far smaller, and unconnected, regions of space and time. This is the basic philosophy behind the hybrid continuum-molecular computational scheme known as the heterogeneous multi-scale method (HMM) [1,2].

In situations where the behaviour at the molecular level can be confidently predicted *a priori*, it is possible to use a full continuum model (as opposed to merely a continuum description) that takes into account the coupled interaction of the molecular processes and the large-scale dynamics. The most common of these models is the traditional Navier–Stokes–Fourier (NSF) equations of fluid dynamics, which bypass the need for a separate molecular description entirely as the molecular behaviour is encompassed in its constitutive closure. The challenge then, in this case, is to identify the regions in space and time where such a model is appropriate, and then to use a full molecular or gas-kinetic description everywhere else. This is a common hybrid approach, known as *domain decomposition*, and is well documented in the literature [3–5].

The topic of the current paper is techniques for time-accurately advancing fluid-molecular hybrids, and methods for exploiting time-scale separation wherever it exists. For unsteady micro and nano flows, disparity in timescales is likely to be even greater than in length scales, and as such, the performance of hybrids methods will depend crucially on the ability to exploit time-scale separation. The methods presented in this paper apply to both HMM *and* domain-decomposition hybrid approaches equally. As such, we do not include a discussion of their relative merits and applicability here; instead, the reader is referred to [2–5] where full reviews of the methods are provided.

It is important to note that a separation in time-scale between molecular processes and the larger scale dynamics does not imply that the NSF equations are valid (i.e. scale separation is a necessary but not sufficient condition to justify the use of the NSF model). One example of this is when the constitutive behaviour of the fluid is unknown (perhaps it is non-Newtonian), requiring molecular simulation at the smallest scales, while a continuum-conservation description is appropriate for flow variation macroscopically. In this case, HMM would be effective. A second example is flow near to surfaces, which could exhibit slip and other near-wall non-equilibrium effects; while there may be time-scale separation between molecule-wall interactions and temporal variations farther from the wall, a molecular or gas-kinetic treatment is still needed near to the surfaces to provide accurate boundary conditions to the bulk flow. In this instance, a domain-decomposition approach would be effective at exploiting the spatial-scale separation, alongside a treatment such as that presented in this paper to exploit the time-scale separation.

In this paper we present a new method for the coupled time-advancement of hybrid solvers, and compare it to existing ones in terms of approximation error and computational efficiency. The paper is structured as follows. In Section 2 existing schemes are described and a new generalised method introduced. In Section 3 approximation and numerical error of each method is discussed and compared, in relation to the solution of a coupled system of ordinary differential equations. We then describe three example applications: in Section 4, the step response of a second-order system composed of two linearly-coupled ODEs; in Section 5 the operation of a popular-design micro-jet actuator; and in Section 6, the unsteady response of a micro bearing to an applied torque. Finally, in Section 7, some conclusions are made and suggestions for further work given.

2. Time-step coupling schemes for hybrid solvers

In this discussion of methods for time advancement in hybrid solvers, we refer to the finest-scale model (e.g. molecular or gas-kinetic) as the *micro* model. The larger-scale model (e.g. a conservation law) is the *macro* model. As the full hybrid model evolves in time, variables are exchanged between the micro and macro models, providing the mechanism by which the systems are coupled; we refer to these as *coupling variables*.

The simplest approach to time advancement in a hybrid framework is to set the time step of the macro model to be that required by the micro model (i.e. much smaller than needed in scale-separated cases); there is then no attempt to exploit scale separation and, as such, the computational cost will very often be much higher than needed. This approach is shown schematically in Fig. 1(a) and we refer to it as the *fully-coupled* approach.

A straightforward improvement to this is to increase the macroscopic time step and exchange macro/micro information less frequently: this time step should be small enough to accurately resolve the variation in coupling variables, but larger than the time-step requirements of the micro model. Fewer exchange instances and macro-model time steps are then needed (see Fig. 1(b)). Since the micro time stepping runs continuously, and the exchange between micro and macro model is intermittent, we refer to this approach as the *CI* method (**C**ontinuous micro solution – **I**ntermittent coupling).

The serious limitation of the CI time-advancement method is that there is no resulting reduction in the number of micro-model time steps that are needed. In the HMM [1], coupling is intermittent but the time-step discretization of the micro model is heterogenous (in keeping with the spatial discretization). Periods in the micro-scale time domain are skipped, as depicted in Fig. 1(c). This is accurate for scale-separated conditions because, after a certain time period, the micro-scale model will be relaxed/equilibrated to any change introduced at the point of coupling. In other words, the micro state's response to the macro state is *quasi steady*. Any micro-time steps beyond such quasi-steady equilibration are, from a computational perspective, wasted; hence they can be skipped without a significant accuracy penalty. For quasi-steadiness to be identified, an estimation is needed of a relaxation period for the micro model, T_{micro}, which characterises the length of time that the micro model requires to equilibrate to any abrupt change in the coupling variables. When there is large scale separation, the macro-scale time step (Δt) is much larger than T_{micro} and large savings can be realised by the omission of wasteful seg-

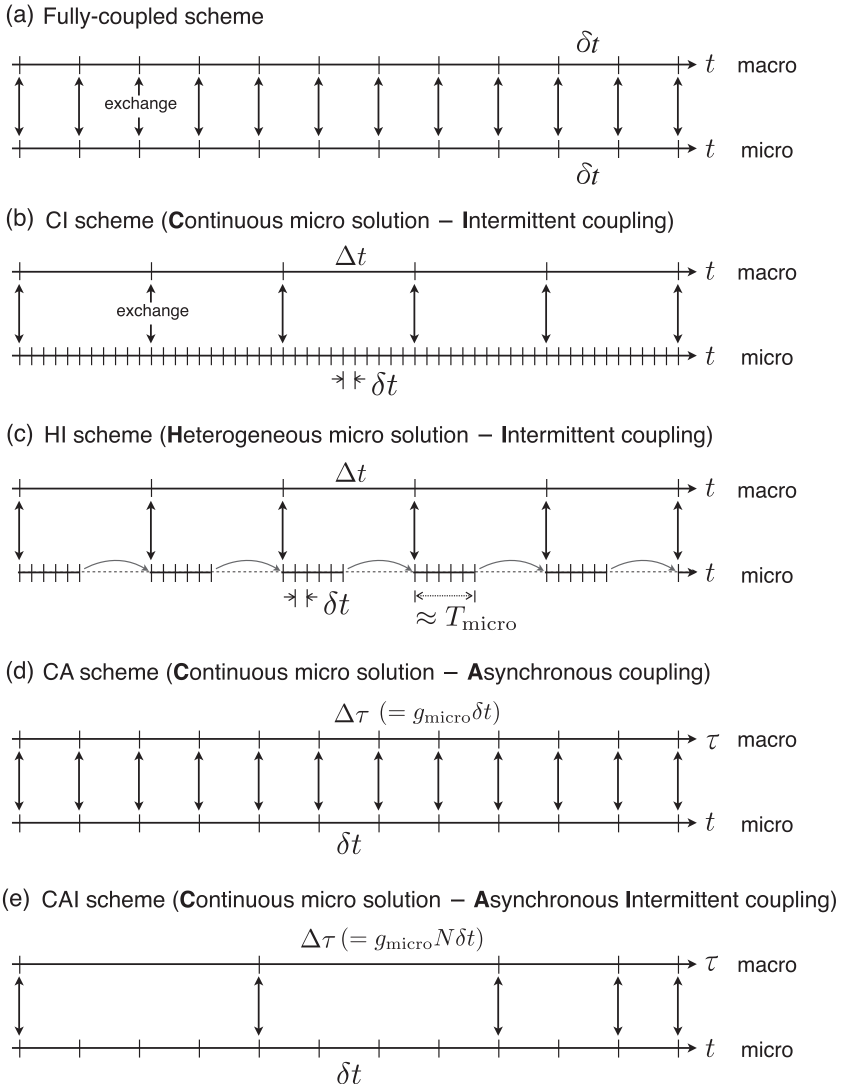

Fig. 1. Schematic of various possible time-step coupling schemes: (a) fully-coupled; (b) CI scheme; (c) HI scheme: HMM [1]; (d) CA scheme: seamless HMM [6]; and (e) new CAI scheme of this paper, where T_{micro} is the micro relaxation period, g_{micro} is the micro gearing, and N is the number of micro-solver steps performed between coupling instances.

ments of the micro-scale time domain. This method we term *HI* (**H**eterogeneous micro solution – **I**ntermittent coupling), (see Fig. 1(c)).[1]

The heterogeneity of the micro time domain in the HI method is potentially a difficulty. In [6] it is suggested that in such a scheme there would be a significant computational overhead due to the fact that the micro model would require re-initialisation after each coupling exchange instance. It is not clear how serious a penalty this is (in fact, re-initialization is arguably not required at all), but the solution proposed (the *seamless* HMM) is particularly elegant and has a number of other attractive features over the HI method. The seamless HMM time-stepping scheme has the micro and macro time-stepping performed continuously ('seamlessly') while exploiting time-scale separation by using a different sized time step in each: δt and $\Delta\tau$, respectively (see Fig. 1(d)); note, although the micro and macro time steps appear equal in the figure, they are drawn along different scales (t and τ). The exchange of data at every time step means that the micro and macro model are actually *asynchronously* coupled; for scale-separated conditions the approximation error this introduces is acceptable, as the micro model remains quasi-steadily equilibrated to the evolving macro state. This method we refer to as *CA* (**C**ontinuous micro solution – **A**synchronous coupling). To preserve generality, and for consistency, we avoid using the term "seamless HMM", which is a combination of a time-stepping and spatial discretization methodology.

The CI, HI and CA methods (Figs. 1(b)–(d)) have their different strengths and weaknesses, which will be discussed in more depth in the next section. However, in this paper we propose an alternative, seeking to combine the best features of each in a generalised procedure. In our new method, asynchronous coupling is performed (as in CA), but with an intermittent coupling

---

[1] We avoid using the acronym 'HMM' to describe this time-advancement technique (even though this is where it originates), since here we are only describing the time-advancement aspect of the methodology, which is applicable to HMM and Domain Decomposition approaches.

(as in HI and CI), allowing a flexible number of micro-solver steps (N) before the exchange of coupling variables; (see Fig. 1(e). We refer to this as the *CAI* method (**C**ontinuous micro solution – **A**synchronous, **I**ntermittent coupling). The number of micro steps, N, provides an additional control, which can be increased where appropriate to lower the cost associated with the coupling instances and the macro-solver time stepping (so approaching the CI and HI methods); and reduced to maximise the range of applicability (so approaching the CA method). The details and benefits of this adaptable approach will be discussed in the following sections.

We first define some properties of the system we are interested in. The independent characteristic time scale for the micro scale model (i.e. the time taken for the variables in the micro model to relax to any step change in the coupled/macro variables) is T_{micro} (as introduced above). The time scale characterising the temporal variation in the macro variables is T_{macro}. A dimensionless *scale-separation number*, S, is the ratio of these two quantities:

$$S = \frac{T_{\text{macro}}}{T_{\text{micro}}}, \tag{1}$$

for $T_{\text{macro}} \geqslant T_{\text{micro}}$. The maximum time-step allowed (either due to accuracy or stability considerations) in each model is related to the two characteristic time scales as follows:

$$\Delta t_{\max} = \frac{T_{\text{macro}}}{n_{\text{macro}}} \quad \text{and} \quad \delta t_{\max} = \frac{T_{\text{micro}}}{n_{\text{micro}}}, \tag{2}$$

where n_{macro} and n_{micro} are the minimum number of time steps required in the macro and micro time period, respectively. Note, for the hybrid models of interest here (e.g. those involving molecular dynamics as the micro model), the micro time step constraint is likely to be dictated by stability considerations rather than accuracy. This might also be true for the macro time-step constraint. The ratio of n_{micro} to n_{macro} gives an indication of the ‘stiffness’ of the models relative to each other:

$$r_{\text{stiff}} = \frac{n_{\text{micro}}}{n_{\text{macro}}}. \tag{3}$$

Typically, for hybrid molecular/continuum methods, $r_{\text{stiff}} \gg 1$; in other words the micro models are much stiffer (i.e. require a much smaller time step as a fraction of their characteristic time) than do the macro models. This has important implications for the computational cost of the various schemes we consider.

Note that, in the time-stepping schemes depicted in Figs. 1(a)–(f), it is assumed that all of the methods employ the same micro time step, i.e. $\delta t = \delta t_{\max}$.

2.1. Gearing of the CI method (Fig. 1(b))

It is often assumed in the literature that, using an HMM approach, the computational cost of a macro model time step is negligible in comparison to the combined cost of the time steps from the micro simulations at each macro model cell. To demonstrate why this is not necessarily the case, consider a full-scale HMM: a hybrid of state-of-the-art computational fluid dynamics (CFD) and molecular dynamics. The CFD simulation has P numerical points/cells in the domain: typically, for an unstructured mesh, the number of computational operations scale with $O(P^3)$ per time step. If the number of molecules in each micro simulation is M, and assuming the intermolecular force calculation is the dominant source of expense, the order of computational operations per time step will scale with $O(M^2)$; the combined expense of all micro simulations (assuming a micro solver at each of the P cells) is then $O(PM^2)$. CFD simulations with as many as $P = 10^9$ cells are becoming typical; while a generous number of molecules per micro simulation would be $M = 10^4$. In such a case the CFD time step would require 10^4 times more operations than the molecular dynamics micro simulations combined, *per time step*. Also considering the fact that the CFD aspect of the simulation is harder to parallelise, and may require re-meshing if the grid is adaptive, it is clear that the cost of a macro time step should not be neglected when evaluating various time-stepping methods for full-scale hybrid methods.

The main benefit of the CI method (Fig. 1(b)) over the fully-coupled solution (Fig. 1(a)) is that a larger macro time step, Δt, can be used, thereby reducing the total number of macro time-steps required in a given simulation period. Moreover, there is also a consequent reduction in the number of coupling instances, which reduces cost related to extracting the coupling variables (e.g. calculating the Irving–Kirkwood stress tensor from the microstructure, an $O(M^2)$ procedure) and the exchange of those variables.

We describe the reduction in computational cost associated with macro time-stepping (from the fully-coupled solution, Fig. 1(a)) as the *macro gearing*, g_{macro}, of the method. For the CI method:

$$g_{\text{macro}} = \frac{\Delta t}{\delta t}. \tag{4}$$

A limit on the macro gearing can be found by the reasonable assumption that $\delta t = \delta t_{\max}$ and $\Delta t \leqslant \Delta t_{\max}$, and from substitution of Eqs. (1)–(3) into Eq. (4), above:

$$g_{\text{macro}} \leqslant r_{\text{stiff}} S. \tag{5}$$

The major limitation, though, of the CI method is that the number of micro time steps performed is identical to that in the fully-coupled case (Fig. 1(a)). We describe the reduction in computational cost associated with micro time stepping (from the fully-coupled solution) as the *micro gearing*, g_{micro}. So, for the CI method, $g_{\mathrm{micro}} = 1$.

2.2. Gearing of the HI method (Fig. 1(c))

In the same way as in the CI method, the HI method (Fig. 1(c)) saves macro time steps because of an intermittent coupling. The macro gearing is thus $g_{\mathrm{macro}} = \Delta t/\delta t$, with the restriction that $g_{\mathrm{macro}} \leqslant r_{\mathrm{stiff}} S$.

However, a fundamental difference is that a physical approximation is made in the HI method to reduce the number of micro time steps calculated. In the fully-coupled and CI methods, the solution converges to the true solution as $\Delta t \to 0$ (assuming a constant r_{stiff}). However, in the HI method, regions of the micro time domain are effectively skipped, which is a physical (as distinct from a numerical) approximation to the true solution. For the HI method, the micro gearing (the reduction in the number of micro-time steps as compared to a fully-coupled solution), is, from inspection of Fig. 1(c):

$$g_{\mathrm{micro}} = \frac{\Delta t}{T_{\mathrm{micro}}}. \tag{6}$$

For a given scale-separated condition, then, in order to change the micro gearing (g_{micro}) the macro time step (Δt) is adjusted. Combining Eqs. (1), (2), (6), with the condition $\Delta t \leqslant \Delta t_{\max}$, gives:

$$g_{\mathrm{micro}} \leqslant \frac{S}{n_{\mathrm{macro}}}, \tag{7}$$

which, given typically that $n_{\mathrm{macro}} \gg 1$, can be a severe restriction on the range of micro gearing that can be applied for a given scale-separated condition. Furthermore, to be at least as efficient as the fully-coupled scheme, $g_{\mathrm{micro}} \geqslant 1$ and therefore, in the lower limit:

$$S \geqslant n_{\mathrm{macro}}. \tag{8}$$

At low to moderate values of S the HI method is therefore not applicable. For problems that exhibit a time-varying degree of scale separation (examples of which are considered later) this is a particular limitation.

2.3. Gearing of the CA method (Fig. 1(d))

The asynchronous coupling of the CA method (Fig. 1(d)) allows regions of the time domain to be skipped at every time step, in effect, continuously. As discussed above, this may have its computational convenience, but it also allows a greater range of applicability. The micro gearing, from inspection of Fig. 1(d), is simply:

$$g_{\mathrm{micro}} = \frac{\Delta\tau}{\delta t}. \tag{9}$$

After substitution of Eqs. (1)–(3) we obtain:

$$g_{\mathrm{micro}} \leqslant r_{\mathrm{stiff}} S; \tag{10}$$

Because, typically, $r_{\mathrm{stiff}} \gg 1$ and $n_{\mathrm{macro}} \gg 1$, Eq. (10) represents a far less severe restriction compared to that on the HI method, Eq. (7).

The macro gearing for the CA method is, in fact, identical to its micro gearing:

$$g_{\mathrm{macro}} = g_{\mathrm{micro}} = \frac{\Delta\tau}{\delta t}, \tag{11}$$

with the same restriction: $g_{\mathrm{macro}} \leqslant r_{\mathrm{stiff}} S$.

The problem is that, as with the HI method, the macro and micro gearing cannot be adjusted independently (they only have one control, Δt and $\Delta\tau$). This means macro gearing cannot be exploited independently of micro gearing. This is an issue if, say, $S \approx 1$ and $r_{\mathrm{stiff}} \gg 1$, because increasing the macro gearing (g_{macro}) to make an appropriate numerical approximation (as in the CI method, Fig. 1(b) would lead to a micro gearing that would introduce an unwanted physical approximation (because the scale separation would not be large enough to warrant it).

2.4. Gearing of the CAI method Fig. 1(e)

In this paper, we propose an alternative to the CI, CA and HI methods, seeking to combine the best features of these within a generalised procedure. Here, asynchronous coupling is performed (as in CA), but intermittently (as in HI and CI), allowing a flexible number of micro-solver steps to be performed between coupling instances; see Fig. 1(e). The number of micro steps, N, provides an additional control allowing the micro gearing to be controlled independently of the macro gearing. As demonstrated later, this enables applicability over a wide range of S, while minimising the number of macro and micro time steps needed. This method we refer to as the *CAI* method.

Inspection of Fig. 1(e) shows that the micro gearing of the CAI method is:

$$g_{\text{micro}} = \frac{\Delta\tau}{N\delta t}. \tag{12}$$

After substitution of Eqs. (1)–(3) we obtain:

$$g_{\text{micro}} \leqslant \frac{r_{\text{stiff}}S}{N}. \tag{13}$$

The macro gearing is simply:

$$g_{\text{macro}} = \frac{\Delta\tau}{\delta t}. \tag{14}$$

The method is, in fact, a generalisation of the previous methods: when $N = 1$ and $g_{\text{micro}} = 1$ it is equivalent to the fully-coupled method (Fig. 1(a)); when $N \geqslant 1$ and $g_{\text{micro}} = 1$ it is equivalent to the CI method (Fig. 1(b)); when $N = n_{\text{micro}}$ and $g_{\text{micro}} \geqslant 1$ it is equivalent to the HI method (Fig. 1(c)); when $N = 1$ and $g_{\text{micro}} \geqslant 1$ it is equivalent to the CA method (Fig. 1(d)). The flexibility provided through the assignment of N enables the best of these methods to be combined in an adaptable manner.

In this paper the assignment of N is made as straightforwardly as possible: to minimise the number of macro time steps performed. As such, it is set as large as the restriction on macro time step will allow (i.e. $\Delta\tau = \Delta t_{\text{max}}$). Combining Eqs. (1)–(3) and (12) gives:

$$N = \frac{r_{\text{stiff}}S}{g_{\text{micro}}}. \tag{15}$$

Since N must be an integer, the real value obtained in Eq. (15) is rounded down, to satisfy (13), or rounded up if it is less than 1.

Eq. (15) ensures that the method has the same range of applicability, in terms of S and g_{micro}, as the CA approach, while reducing the macro time steps performed by as much as possible (by maximising g_{macro}). Combining Eqs. (12), (14), (15) gives:

$$g_{\text{macro}} = r_{\text{stiff}}S. \tag{16}$$

2.5. Summary of methods

Table 1 summarises the range and applicability of the various methods discussed so far; the three key features are presented: (1) the micro gearing range; (2) the applicable range of scale separation; (3) the range of N (it is only in the CI and CAI method that this is independently controllable). As can be seen by comparison, the CAI method combines the desirable features of all methods: the range of micro gearing is as large as the CA method; it is applicable down to $S = 1$; and the number of macro time steps per coupling instance can be controlled independently, enabling macro efficiency to be maximised.

Despite the marked differences in the characteristics of these methods, they can be implemented using the same general time-stepping algorithm. To help describe this algorithm we introduce an abstract representation of a multiscale system consisting of a pair of coupled equations:

$$\partial_t U = F(U; \gamma(u)) \quad (\text{macro}) \tag{17}$$

$$\partial_t u = f(u; \Gamma(U)) \quad (\text{micro}) \tag{18}$$

with initial conditions

$$U(0) = U^0, \quad u(0) = u^0,$$

where U are the macro-state variables, u are the micro-state variables, and the operators F and f represent the macro and micro models, respectively. The operators Γ and γ represent any model for the processing of variables passed between the macro and micro models.

Table 1
Summary of properties of the time-stepping methods in Figs. 1(a)–(e)

Method	Figure	g_{micro}	Applicable S	$N(=g_{\text{macro}}/g_{\text{micro}})$
Fully-coupled	Fig. 1(a)	Fixed = 1	$\geqslant 1$	Fixed = 1
CI	Fig. 1(b)	Fixed = 1	$\geqslant 1$	$\geqslant 1$
HI	Fig. 1(c)	$\leqslant S/n_{\text{macro}}$	$\geqslant n_{\text{macro}}$	Fixed $= n_{\text{micro}}$
CA	Fig. 1(d)	$\leqslant r_{\text{stiff}}S$	$\geqslant 1$	Fixed = 1
CAI	Fig. 1(e)	$\leqslant r_{\text{stiff}}S$	$\geqslant 1$	$\geqslant 1$

```
Require: $U^t$, $u^t$, $\delta t$, $g_{\mathrm{micro}}$, $N$          ▷ the variables needed to complete a macro time step
  $q \leftarrow 0$
  repeat
      $u^{t+(q+1)\delta t} \leftarrow u^{t+q\delta t} + \delta t\, f(u^{t+q\delta t}\,; \Gamma(U^t))$          ▷ perform a micro time step
      $q \leftarrow q + 1$
  until $q = N$
  $\Delta t \leftarrow g_{\mathrm{micro}} N \delta t$
  $u^{t+\Delta t} \leftarrow u^{t+N\delta t}$          ▷ make the physical approximation
  $U^{t+\Delta t} \leftarrow U^t + \Delta t\, F(U^t\,; \gamma(u^{t+\Delta t}))$          ▷ perform a macro time step
  $t \leftarrow t + \Delta t$          ▷ update the macro time
```

Fig. 2. Coupling algorithm for a macro time step; general to all coupling schemes in Fig. 1 (see Table 1 for values of g_{micro} and N for each scheme). q is an index for a loop around the micro solver. This example uses an explicit Euler method for the macro and micro models, individually.

For simplicity, let us assume that an explicit Euler method is to be used for time advancement of the equations individually. For the case of a fully-coupled scheme (Fig. 1(a)) this leads to a sequential time-stepping procedure for the solution of Eqs. (17) and (18) as follows:

$$U^{t+\delta t} = U^t + \delta t\, F(U^t; \gamma(u^t)) + O(\delta t^2), \tag{19}$$

$$u^{t+\delta t} = u^t + \delta t f(u^t; \Gamma(U^t)) + O(\delta t^2), \tag{20}$$

where the superscripts t and $t + \delta t$ refer to the state of the variables at that particular instant. Using the same notation a general algorithm for a single macro time step is presented in Fig. 2; this is applicable to all five of the coupling schemes in Fig. 1. (Note, truncation error terms from the explicit Euler method have been omitted).

3. Physical approximation and numerical error

As noted above, the micro gearing (i.e. the factor reduction in number of micro time steps computed) is afforded by a physical approximation, which has an error associated with it. This is distinct from error arising from the particular numerical discretisation adopted. As a starting point for investigating both these physical and numerical errors, we consider a coupled system of ordinary differential equations, which together constitute a classic forced-oscillator problem:

$$\frac{\mathrm{d}x}{\mathrm{d}t} = -ky + e^{\mathrm{i}\omega t}, \quad \text{(macro)} \tag{21}$$

$$\frac{\mathrm{d}y}{\mathrm{d}t} = -cy + x, \quad \text{(micro)} \tag{22}$$

where x and y are the macro and micro variables, respectively; and c, k are real valued constants. Analytical solutions for the macro variables, x and y, are of the form:

$$x = Ge^{\mathrm{i}\omega t}; y = He^{\mathrm{i}\omega t}, \tag{23}$$

where

$$G = \frac{\mathrm{i}\omega + c}{k + \mathrm{i}c\omega - \omega^2} \quad \text{and} \quad H = \frac{1}{k + \mathrm{i}c\omega - \omega^2}. \tag{24}$$

The natural frequency of the coupled system is given by $\omega_n = \sqrt{k}$ and the damping factor $\zeta = c/(2\omega_n)$. In order to estimate the degree to which this coupled system is time-scale separated, we need to express characteristic times for the macro and micro equations independently of each other (as if they were decoupled):

$$T_{\mathrm{macro}} = 1/\omega \quad \text{and} \quad T_{\mathrm{micro}} = 1/c. \tag{25}$$

Note, we have assumed in this particular definition of T_{macro} that $\omega > \omega_n$. The temporal scale-separation number given in Eq. (1) is then:

$$S = \frac{c}{\omega}. \tag{26}$$

3.1. Error due to physical approximation

For the simple equation system (21) and (22), the error due to the physical approximation (where $g_{\mathrm{micro}} > 1$) can be considered separately to any numerical error. The fully-coupled and CI methods make no physical approximation to the micro relaxation behaviour, but clearly save no computational micro time steps either, and are thus not considered here. The micro gearing approximations of the remaining three methods (HI, CA, and CAI) are all equivalent (assuming that for the HI method the heterogeneous micro solvers are initiated using information from the previous micro solution, as depicted in Fig. 1(c)). This approximation (and consequent computational saving) results from solving the macro and micro equations, in effect, on different time scales (τ and t, respectively), where the ratio between these two is the micro gearing, g_{micro}, which for each method is defined by Eqs. (6), (9), (12). The equivalent system of equations, with micro gearing, is then:

$$\frac{\mathrm{d}x}{\mathrm{d}\tau} = -ky + e^{i\omega\tau}, \quad (\text{macro}) \tag{27}$$

$$\frac{\mathrm{d}y}{\mathrm{d}t} = -cy + x, \quad (\text{micro}) \tag{28}$$

where $\tau = g_{\text{micro}}t$. The analytical solution to these coupled equations is of the same form as in Eq. (24) but with

$$G = \frac{g_{\text{micro}}i\omega + c}{k + ic\omega - g_{\text{micro}}\omega^2} \quad \text{and} \quad H = \frac{1}{k + ic\omega - g_{\text{micro}}\omega^2}. \tag{29}$$

In the next section we show that numerical solutions to the original equations (21, 22) converge to this solution for each of the HI, CA and CAI methods.

By comparing the full solution (24) with the approximate solution (29) it can be seen they approach each other if $c \gg \omega g_{\text{micro}}$ for $g_{\text{micro}} > 1$. From Eq. (26) it can be seen that these conditions occur at high scale separation, i.e., when $S \gg g_{\text{micro}}$.

Fig. 3 shows the mean error (i.e., departure from the full solution (24)) of the amplitudes of x and y given by the approximate solution (29), for a range of degrees of scale separation S at gearing g_{micro} = 2, 10 and 20. Two cases are considered, at greatly different normalised frequencies ω/ω_n; the results from these two cases are essentially the same. As expected, as S

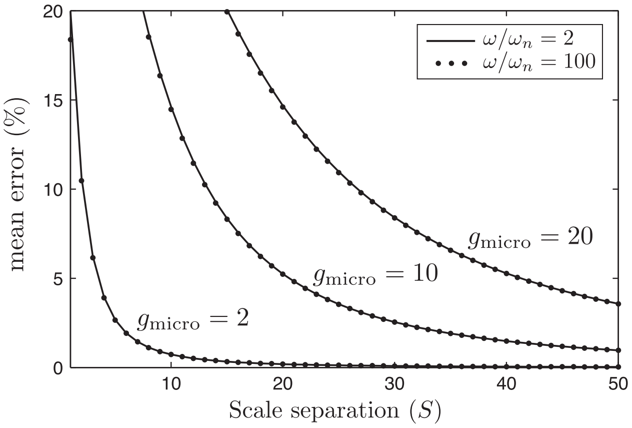

Fig. 3. Mean error of the amplitudes of x and y given by Eq. (29), for a range of degrees of scale separation S, at gearings g_{micro} = 2, 10 and 20; ω/ω_n = 2: (—), and ω/ω_n = 100: (⋯).

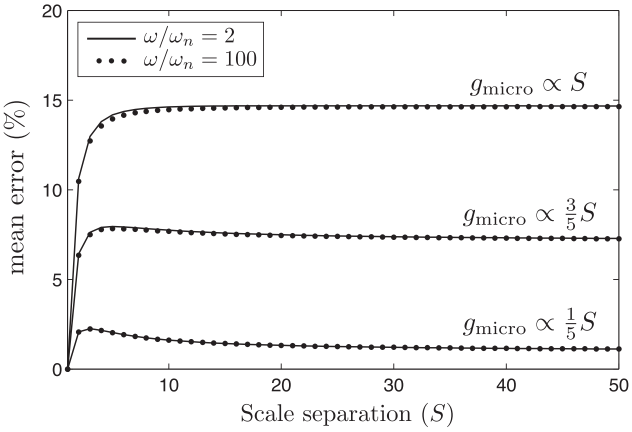

Fig. 4. Mean error of the amplitudes of x and y given by Eq. (29), for a range of degrees of scale separation S, at gearing given by $g_{\text{micro}} = k_g(S-1)+1$. For k_g = 1, 3/5, and 1/5; ω/ω_n = 2: (—), and ω/ω_n = 100: (⋯).

increases the error of the approximate solution reduces. At higher S, this means that a larger g_{micro} can be afforded for the same level of error. Given this general observation, and anticipating that in problems with varying scale separation it is desirable to have a reasonably consistent level of error, we propose that the micro gearing be set in proportion to the scale separation, i.e.:

$$g_{\mathrm{micro}} = k_g(S-1)+1, \tag{30}$$

where k_g is a constant of proportionality that acts as a control on how aggressively scale separation is exploited at the expense of accuracy. Fig. 4 presents the same mean error calculation as in Fig. 3 but with the micro gearing, g_{micro}, set by Eq. (30). The results indicate, at least for the two cases considered, our proportional scaling of g_{micro} with S is an effective way of maximising the micro gearing, while keeping the error level bounded, over a wide range of scale separation.

3.2. Error due to numerical discretization

In this subsection the two ODEs (21) and (22) are solved numerically. For consistency, both the micro and macro equations are advanced using an implicit scheme with second-order accuracy (a standard combination of forward and backward Euler methods). In the first instance, the exchange of coupling variables in each method is performed as depicted in Fig. 1, where the transfer of information between the micro and macro solver is *simultaneous* (as described in [4]). Fig. 5(a) shows a plot of mean error in x and y amplitude predictions (compared to the analytical solution (24)) obtained using the fully-coupled solution, with increasing time step δt. For this case $S = c = \omega = 1$. The results indicate that with simultaneous exchange of coupling variables (the circles in Fig. 5(a)) the numerical error of the method scales linearly with the time step, i.e., it is first-order accurate. A similar plot is obtained for the CI method (using $g_{\mathrm{macro}} = 40$) in Fig. 5(b), demonstrating that despite the macro step being 40 times larger than the micro time step in this example, first-order accuracy is still achieved (g_{macro} is constant with varying δt).

In calculating the numerical error for the CA, HI and CAI methods we compare with the approximate analytical solution in Eq. (29). In the case selected here, $g_{\mathrm{micro}} = 4$. For the CA method, the macro time step, $\Delta\tau$, is set by Eq. (9); for the CAI method, the macro time step is set by Eq. (12) with $N = 40$. The CAI method is equivalent to the HI method in the case $N = n_{\mathrm{micro}}$; as such, we do not need to consider the numerical error of the HI method separately. Figs. 6(a) and (b) indicate that the methods are also all first-order accurate if variable exchange occurs simultaneously (note, this is accuracy in achieving the approximate solution, which is based on a physical assumption, as discussed in Section 3.1).

As an alternative to the simultaneous exchange of coupling variables depicted in Figs. 1(a)–(e), we also propose a staggered exchange, termed *leapfrog* coupling. This concept is illustrated in Figs. 7(a) and (b) for the fully-coupled and the CAI method, respectively. Note that, in the context of the description in [4], this is a sequential scheme; the important distinction being it is also staggered. The triangle symbols in Figs. 5(a), show that by using leapfrog coupling, the second-order accuracy of the micro and macro solvers, individually, is retained in the coupled solutions. This second-order accuracy depends, of course, on the particulars of the numerics of the micro and macro solvers, and how the coupling variables are used in each model. However, it is likely that such leapfrog coupling will provide an accuracy improvement on the standard simultaneous exchange approach, with no computational penalty. This increased accuracy arises because, when advancing the macro solver, the coupling variable from the micro solver provides information at the half point between the current and

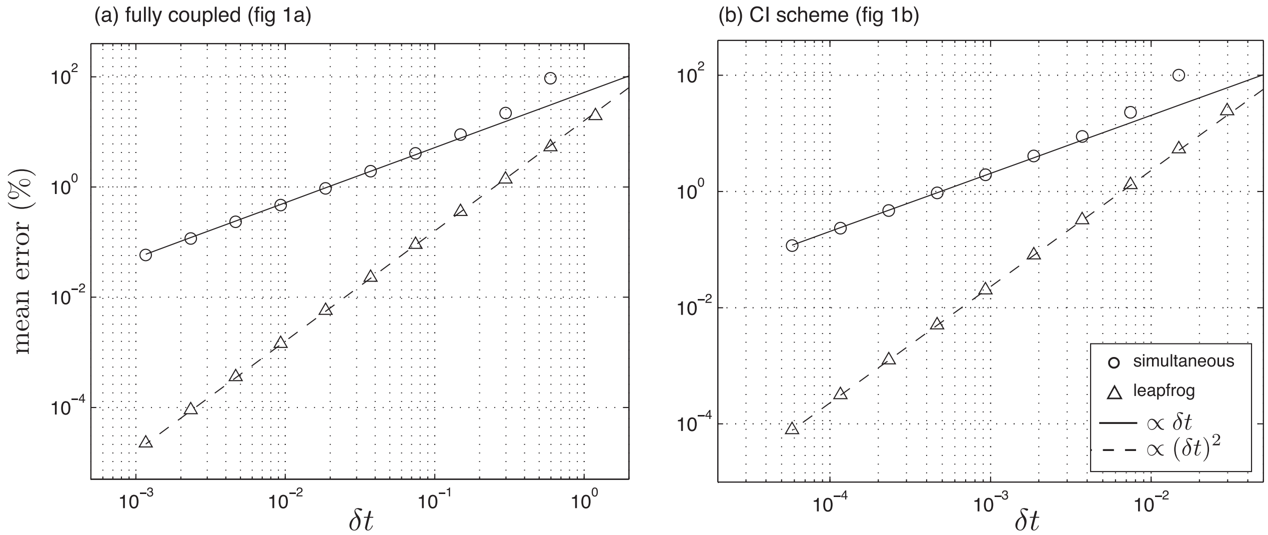

Fig. 5. Mean error in x and y amplitude predictions from the analytical solution (24), against micro time step δt. Comparison of (a) fully-coupled scheme (see Fig. 1(a) and (b) the CI scheme (see Fig. 1(b) with $g_{\mathrm{macro}} = 40$). The solid and dashed lines (plotted for visual guides) are linear and quadratic functions of δt, respectively.

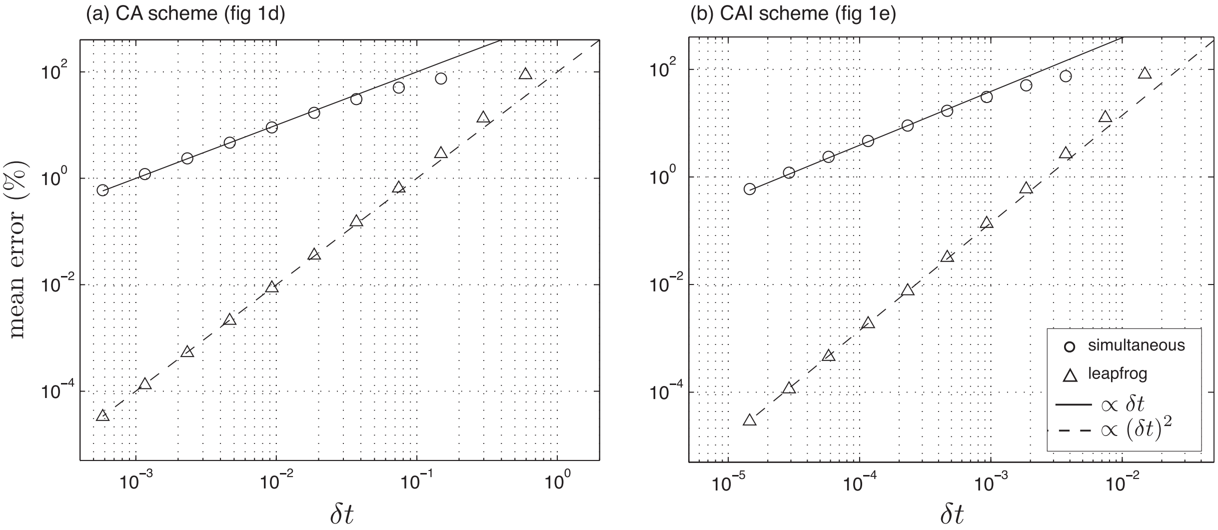

Fig. 6. Mean error in x and y amplitude predictions from the approximate analytical solution (29), against micro time step δt. Comparison of (a) CA scheme (see Fig. 1(d)) with $g_{\text{micro}} = 4$ and (b) the CAI scheme (see Fig. 1(e)) with $g_{\text{micro}} = 4$ and $N = 40$. The solid and dashed lines (plotted for visual guides) are linear and quadratic functions of δt, respectively.

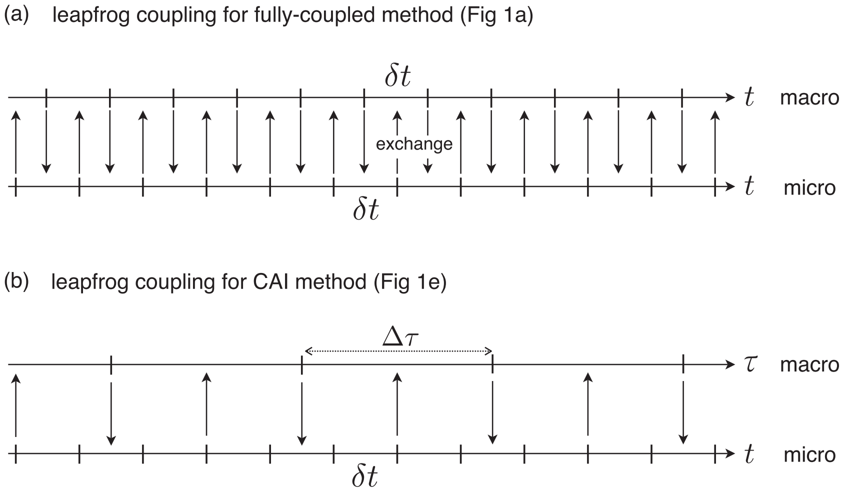

Fig. 7. Schematic of leapfrog coupling for (a) the fully-coupled method, and (b) the CAI method.

the next macro time step. A general algorithm for perfoming a macro time step is presented in Fig. 8 for leapfrog coupling (in terms of the abstract multiscale system introduced in Section 2.5); in this example a first-order explicit Euler method is used for the macro and micro models, individually.

All of the remaining simulations presented in this paper adopt leapfrog coupling.

4. Example I: step response of coupled ODEs

We now consider the first of three example applications of the HI, CA and CAI schemes for $g_{\text{micro}} > 1$ (the fully-coupled and CI scheme are not considered, since for these schemes $g_{\text{micro}} = 1$). Having established in Sections 3.1 and 3.2 that the physical approximation, as well as the order of numerical error, is the same for the HI, CA and CAI schemes, the comparison here is focussed on range of applicability and computational expense.

Our first example, chosen mainly for simplicity, is the step response of a coupled system of ODEs:

$$\frac{dx}{dt} = -ky, \quad (\text{macro}) \tag{31}$$

$$\frac{dy}{dt} = -cy + x, \quad (\text{micro}) \tag{32}$$

where k and c are real-valued coefficients. Although individually the equations are first-order, the coupled system represents a classic second-order system, where the natural frequency is $\omega_n = \sqrt{k}$ and the damping factor $\zeta = c/(2\omega_n)$. Fig. 9(a) shows the evolution of the variable y from the initial conditions $y(0) = 0$ and $x(0) = 1$, with $\zeta = 2.72$ and $\omega_n = 0.184$; this is a fully-coupled numerical solution. The response of y is characterised by a very rapid initial increase, followed by a much more gradual decay to zero. As such, it is less likely that the system will be scale-separated during the initial stage, as compared to the latter stages.

For problems such as this, where the degree of scale separation varies as the system evolves, we define a *local scale-separation* number (analogous to the local Knudsen number for rarefied gas flows, e.g. [7,8]) that compares the shortest relaxation time scale of the system (T_{micro}) with a time scale that characterises the evolution of the coupling variables:

$$S = \min\left\{ \frac{x_{\text{ref}}}{T_{\text{micro}}} \left|\frac{\mathrm{d}x}{\mathrm{d}t}\right|^{-1}, \frac{y_{\text{ref}}}{T_{\text{micro}}} \left|\frac{\mathrm{d}y}{\mathrm{d}t}\right|^{-1} \right\}, \tag{33}$$

where the derivative terms can be evaluated at the beginning of each macro time step using backward Euler differencing, and x_{ref} and y_{ref} are reference values characterising the range of values of the respective variables envisaged within the simulation (an estimation is sufficient). These reference values are needed (as they are with local Knudsen numbers) to identify what should be considered a significant variation in the variables' magnitude. Note, in this new definition of scale separation, T_{macro}, which features in Eq. (1), has been replaced by an instantaneous measure of the rate of evolution of the coupling variables. For this example, $T_{\text{micro}} = 3/c$.

A plot of S, estimated using Eq. (33), is shown in Fig. 9(b) for the case presented in Fig. 9(a); the initial period of rapid development is indeed characterised by a low S value, while at later stages, S increases steadily.

In performing simulations of this system with the HI, CA and CAI schemes, the expression for S in Eq. (33) is evaluated at the beginning of each macro time step, and the micro gearing g_{micro}, which varies proportionally with S, is calculated from Eq. (30). In general, for problems having varying time scale separation (such as this one and those of Section 5.4 and Section 6) the algorithms presented in Figs. 2 and 8 only need to be adjusted to reflect the recalculation of S, g_{micro} and N at the beginning of each macro time step.

```
Require: $U^t$, $u^{t-\Delta t/2}$, $\delta t$, $g_{\text{micro}}$, $N$        ▷ the variables needed to complete a macro time step
  $q \leftarrow 0$
  repeat
      $u^{t+(q+1-N/2)\delta t} \leftarrow u^{t+(q-N/2)\delta t} + \delta t\, f(u^{t+(q-N/2)\delta t}; \Gamma(U^t))$        ▷ perform a micro time step
      $q \leftarrow q + 1$
  until $q = N$
  $\Delta t \leftarrow g_{\text{micro}} N \delta t$
  $u^{t+\Delta t/2} \leftarrow u^{t+N\delta t/2}$        ▷ make the physical approximation
  $U^{t+\Delta t} \leftarrow U^t + \Delta t\, F(U^t; \gamma(u^{t+\Delta t/2}))$        ▷ perform a macro time step
  $t \leftarrow t + \Delta t$        ▷ update the macro time
```

Fig. 8. Leapfrog coupling algorithm for a macro time step; general to all coupling schemes in Fig. 1 (see Table 1 for values of g_{micro} and N for each scheme). q is an index for a loop around the micro solver. This example uses an explicit Euler method for the macro and micro models, individually.

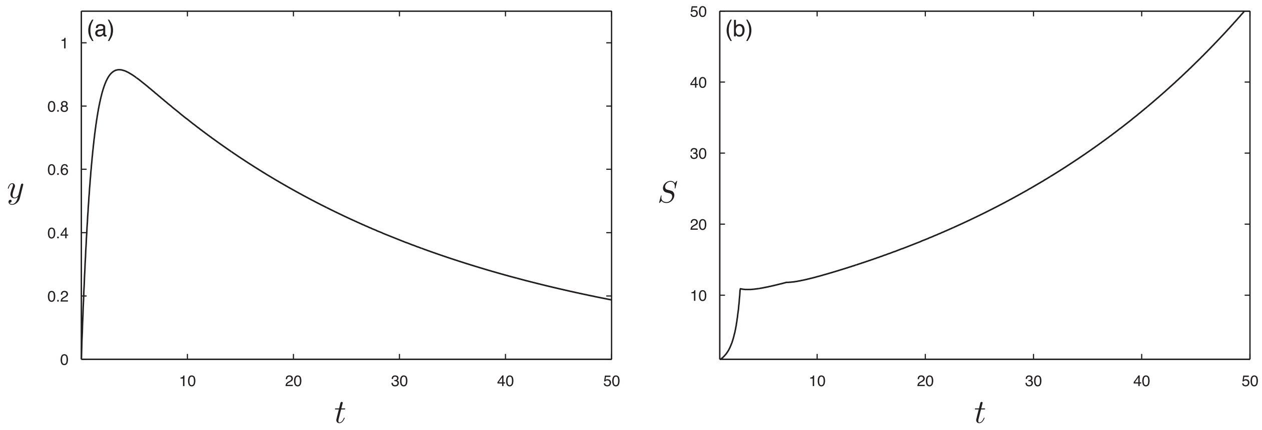

Fig. 9. Step response of the coupled ODE system (31), (32) solved numerically using the fully-coupled scheme. Plots of (a) y against t and (b) local scale separation, S, evaluated from Eq. (33), against t.

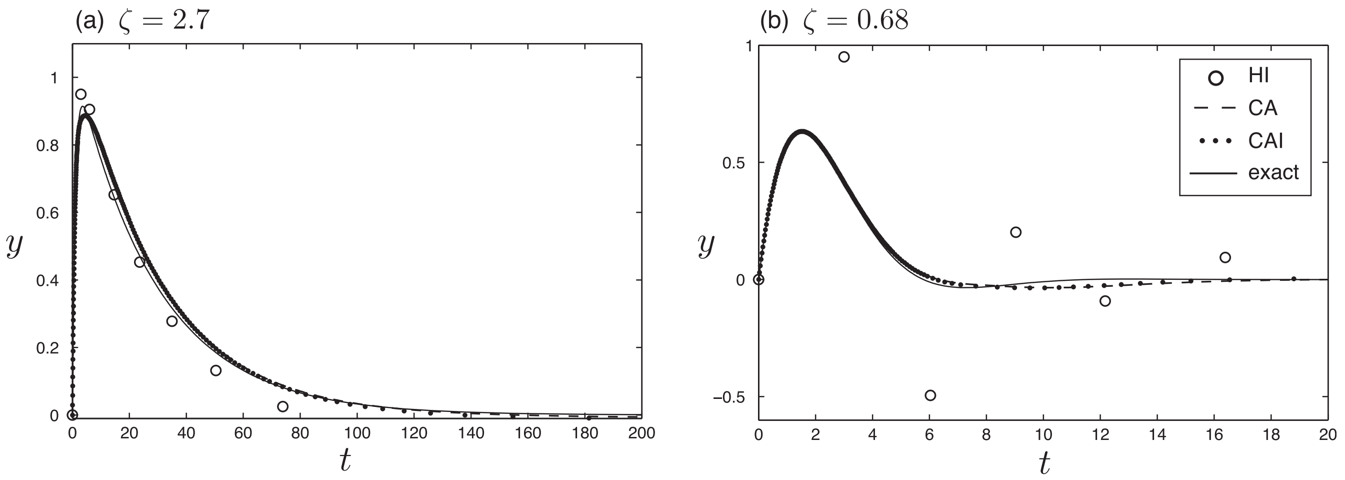

Fig. 10. Step response (y against t) of the coupled ODE system (31) and (32) for (a) $\zeta = 2.7$ and (b) $\zeta = 0.68$, solved numerically using the HI (∘), CA (– –), and CAI (···) schemes. The solid line is the exact analytical solution.

Table 2
Values for macro and micro components of computational speed-up (based on the factor reduction in time-step operations as compared to a fully-coupled solution) for simulations presented in Fig. 10 using the HI, CA and CAI schemes.

Method	Micro speed-up ($\zeta = 2.7$)	Macro speed-up ($\zeta = 2.7$)	Micro speed-up ($\zeta = 0.68$)	Macro speed-up ($\zeta = 0.68$)
HI	7.8	820	1.2	130
CA	13	13	2.7	2.7
CAI	13	35	2.7	3.7

Fig. 10(a) shows results for each scheme, with $k_g = 1/5$, $x_{\text{ref}} = 1$, $y_{\text{ref}} = 1$, and $r_{\text{stiff}} = 1$. The results from the CA and CAI are barely distinguishable, and are both close to the analytical solution. The HI method, though, suffers from lack of resolution macroscopically. This is more evident in Fig. 10(b), which shows results for a case with sub-critical damping ($\zeta = 0.68$, $\omega_n = 0.184$). The reason for this lack of accuracy is that in these two cases the HI scheme is being used outside its applicable range. This range of applicability, summarised in Table 1 for each of the methods, is determined by the maximum acceptable macro time-step size; i.e., in Figs. 10(a) and (b) the macro time step is too large in the HI scheme.

Table 2 details the computational speed up of each of the methods in terms of the factor reduction (from a fully-coupled solution) of the macro and micro computations performed in each simulation. The speed-up of the HI method can, given its unacceptable accuracy, be discounted. The important comparison, then, is that between the CA and CAI schemes. In both cases, the methods have essentially the same accuracy (which is expected, as discussed earlier) and demonstrate the same computational speed-up in terms of micro computations performed. However, in both test cases the CAI method provides a greater speed up in terms of macro computations: almost 3× faster than the CA method in the over-damped case.

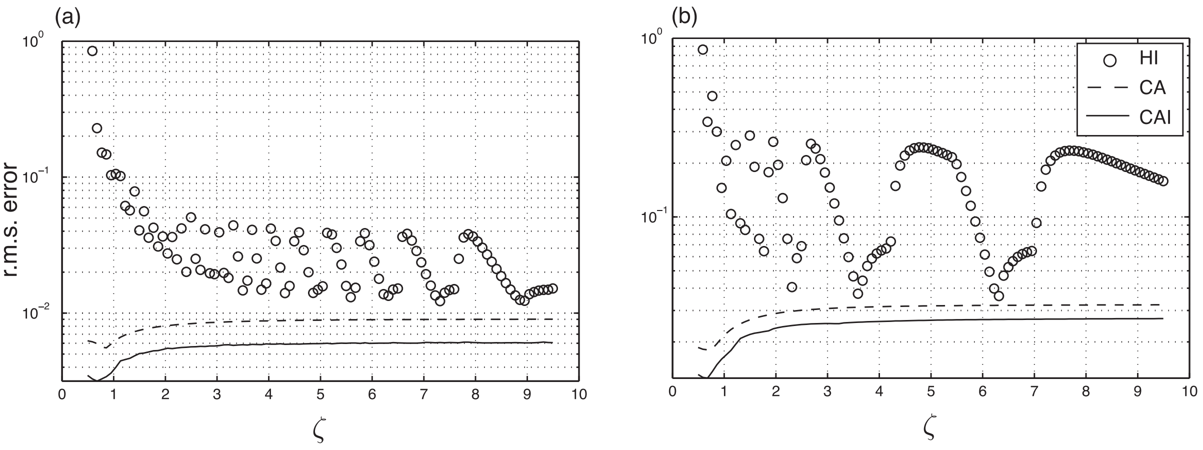

Fig. 11. The root mean squared of the difference between the exact analytical solution and the HI (∘), CA (– –), and CAI (—) solutions. For (a) $k_g = 1/20$; and (b) $k_g = 1/5$.

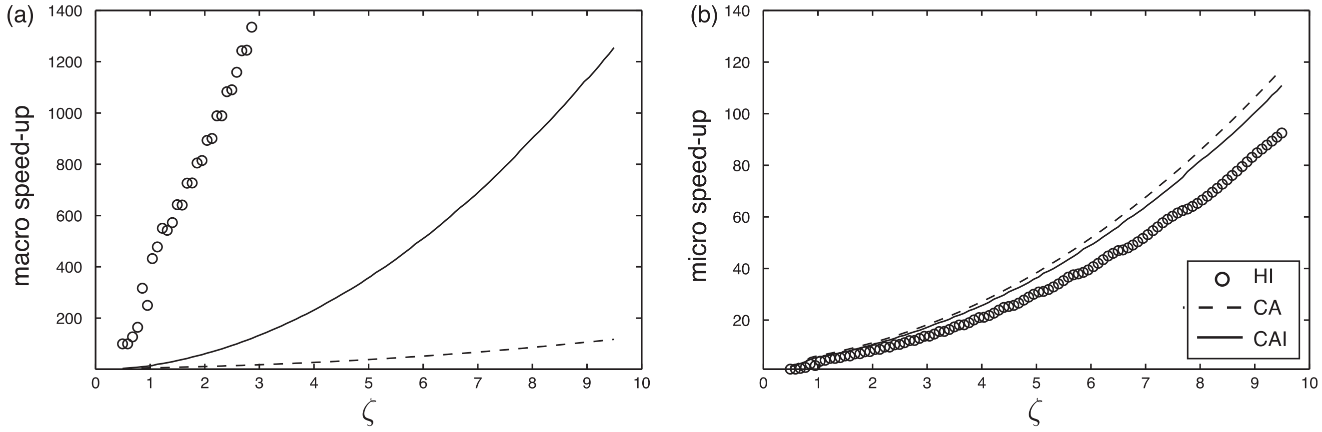

Fig. 12. (a) Macro and (b) micro components of computational speed-up (based on the factor reduction in time-step operations as compared to a fully-coupled solution). Comparison of the HI (∘), CA (– –), and CAI (—) schemes for $k_g = 1/20$.

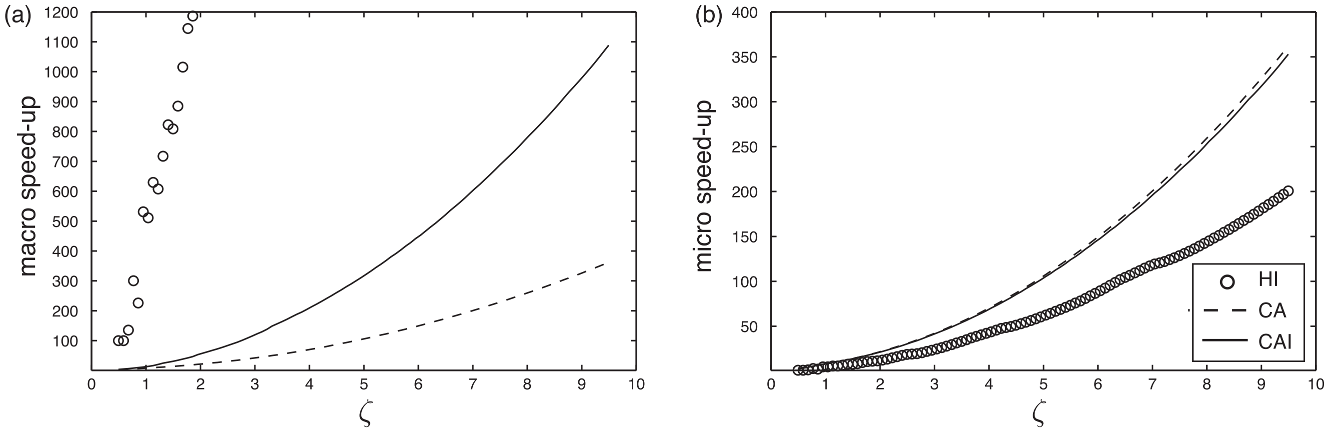

Fig. 13. (a) Macro and (b) micro components of computational speed-up (based on the factor reduction in time-step operations as compared to a fully-coupled solution). Comparison of the HI (∘), CA (– –), and CAI (—) schemes for $k_g = 1/5$.

Simulations are now performed over a range of ζ values (with $\omega_n = 0.184$), and the r.m.s. of the difference between the multiscale result and the analytical solution is calculated over the time period $40\zeta/\omega_n$, for each case. Figs. 11(a) and (b) show the r.m.s. error, for the HI, CA and CAI schemes for conservative ($k_g = 1/20$) and moderate ($k_g = 1/5$) gearing, respectively. As in the results of Fig. 10, the HI provides a far less accurate solution, particularly for low damping factors: in some cases the r.m.s. error is of equivalent magnitude to the initial value of y.

The CA and CAI schemes are comparably accurate, although the error of the CAI scheme is consistently lower. Figs. 12(a) and (b) show the speed-ups in terms of macro and micro computations, respectively, for $k_g = 1/20$. Figs. 13(a) and (b) show the speed-ups for $k_g = 1/5$. Again, since the HI method is out of its applicable range (evidenced by the magnitude of the error), we can discount the very large macro speed ups obtainable using this approach. More importantly, what can be seen from Figs. 12(a) and (b), 13(a) and (b) is that the speed-up of the CAI method is either comparable to, or much greater than, the speed-up from the CA method. For very large levels of damping, for $k_g = 1/20$, the macro speed-up of the CAI method is over $10\times$ greater than in the CA method; moreover, the CAI method produces a *more accurate* result.

Note, that the reason why the methods obtain different levels of micro speed-up, despite g_{micro} being set using the same expression (30), is that the numerical evaluation of the derivative in S is slightly different in each case.

5. Example II: a micro-jet actuator

A generic design of the micro-jet actuators currently being studied for flow-control applications [9–14] as well as cooling applications [15], is depicted in Fig. 14. Its mode of operation is straightforward. An electric field is applied to a piezoceramic driver, which then contracts to force the diaphragm upwards. This reduces the volume of the plenum chamber, raising the plenum pressure p which then drives a jet out through the exit orifice (into a boundary layer, say). If an oscillating electric

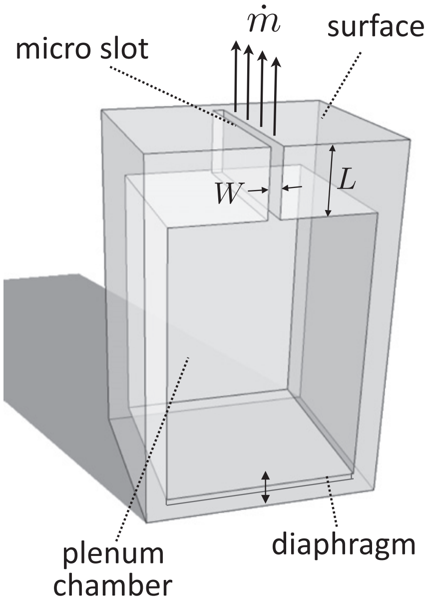

Fig. 14. Cross-section of a generic micro-jet actuator.

field is applied to the driver, the diaphragm oscillates up and down, producing a so-called *synthetic jet* [9–11,15]. Alternatively, if a unidirectional electric field is applied to the driver, the diaphragm only deflects upwards to produce a kind of pulsed jet [12–14]; following [13] this mode of operation is called *pressure-jump* actuation. In either mode of operation, processes occurring in the plenum and slot are intrinsically coupled (the mass flow rate through the slot affects the plenum pressure, and vice versa) while each act over greatly different time and space scales. The flow velocities in the plenum are likely to be slow enough to be safely ignored, while in the micro-scale slot rarefaction will mean that complex non-equilibrium effects (e.g. Knudsen layers) need to be resolved.

Here we construct a simple domain decomposition hybrid model (to exploit spatial scale separation), which will be solved in conjunction with the HI, CA and CAI time-stepping schemes (to exploit time-scale separation). The domain is decomposed into the plenum and slot regions: in the plenum we solve a ‘macro’ equation (derived from mass conservation and the equation of state for an ideal gas); in the slot we solve a ‘micro’ equation (the BGK-Boltzmann equation).

5.1. The macro model

The temporal evolution of the pressure within the plenum can be described by a simple ODE, as in [11,13,14]:

$$\frac{dp}{dt} = -\frac{1}{V_\mathrm{p}}\left(\dot{m}RT + p\frac{dV_\mathrm{p}}{dt}\right), \tag{34}$$

where $\dot{m}$ is the mass flow rate exiting the device, V_p is the volume of the plenum, R is the gas constant and T is the fixed temperature within the plenum. This equation is derived from mass conservation and the assumption of an ideal stationary gas undergoing isothermal compression (see [13] for more details). For this example, we take the geometry of the actuator to be two-dimensional, in that the cross-section of the slot and plenum is constant (as depicted in Fig. 14). If the slot length L is significantly larger than the slot width W the pressure gradient Π is approximately constant over the length of the slot:

$$\Pi = \frac{p_\mathrm{ext} - p}{L}, \tag{35}$$

where p_ext is the pressure external to the device, assumed to be constant. Eqs. (34) and (35) can be combined to give an equation for the evolution of the pressure gradient:

$$\frac{d\Pi}{dt} = \frac{1}{LV_\mathrm{p}}\left(\dot{m}RT + (p_\mathrm{ext} - \Pi L)\frac{dV_\mathrm{p}}{dt}\right). \tag{36}$$

This equation constitutes the macro model. In the simulations of this section, individual time steps of Eq. (36) are calculated using an implicit second-order Euler scheme.

5.2. The micro model

For micro gas flows, such as that through the slot of the micro actuator in Fig. 14, rarefaction effects can potentially dominate the fluid behaviour [7]. The conventional way to express the degree of gas rarefaction of a flow is the Knudsen number:

$$\mathrm{Kn} = \frac{\lambda}{l}, \tag{37}$$

where λ is the mean free path between molecular collisions and l is some characteristic length scale of the flow (in this example, the width of the slot, i.e., $l = W$). For high Knudsen number flows (greater than approximately $\mathrm{Kn} = 10^{-2}$) the Navier–Stokes equations become inaccurate, and a kinetic-based treatment is usually required. In this example we solve an approximate form of the Boltzmann equation (the Bhatnager-Gross-Krook model), which has been applied extensively in the field of rarefied gas dynamics (e.g. [16–19]). For the example of flow through the slot (i.e. channel flow) the BGK-Boltzmann equation is as follows:

$$\frac{\partial f}{\partial t} + c_y \frac{\partial f}{\partial y} + \frac{F_x}{\mathcal{M}} \frac{\partial f}{\partial c_x} = \frac{f^{\mathrm{eq}} - f}{\tau_{\mathrm{r}}}, \tag{38}$$

where x is a coordinate in the bulk flow direction, y is a coordinate perpendicular to the flow (in the direction of the slot width, W), f is the molecular probability distribution function, f^{eq} is the equilibrium distribution function, τ_{r} is the molecular relaxation time, F_x is an external force in the flow direction, $\mathcal{M}$ is the molecular mass, and c_x and c_y are molecular velocities in the x and y directions, respectively. Provided the pressure drop over the slot length is not too large (in keeping with the linearity of the BGK method), we can model the pressure gradient generated by the macro model Π via an external force $F_x = \Pi/\rho_n$, where ρ_n is the number density.

A discrete velocity method is used to solve a standard reduced form of Eq. (38), which reduces the components of phase space over which the distribution function need be calculated: only one molecular velocity component, one spatial component, and time are required. The reader is referred to [18,19] for a detailed description of the mathematical and numerical formulation of this method. For numerical integration over molecular velocity space, Gaussian quadrature is used, and temporal discretization is performed using a standard second-order accurate Lax–Wendroff scheme. For all simulations in Section 5 and Section 6, there are 100 grid points in the y direction, 80 discrete velocities, and a time step just small enough to ensure stability.

The mass flow rate of the gas through the slot can be calculated from the solution of the molecular distribution function f. First, the macroscopic velocity of the gas is obtained from the first-order moment of f, and then the mass flow rate calculated by integrating this macroscopic velocity over the cross-section of the slot. The mass flow rate (per unit length), for this particular example, can be expressed as:

$$\dot{m}(t) = \mathcal{M} \int_0^W \int \int_{-\infty}^{\infty} \int c_x f(t, y, \mathbf{c}) \mathrm{d}\mathbf{c} \mathrm{d}y \tag{39}$$

where $\mathbf{c}$ is the molecular velocity vector and the triple integral is over all of molecular velocity space. Note, by using the reduced form of (38) as discussed above, numerical integration over velocity space only needs to be performed over one dimension. This flow rate $\dot{m}$ is a coupling variable, and is passed to the macro model (36) at the half-way point of the macro time step, as indicated in Figs. 7 and 8. For each slot width (i.e., each value of Kn considered) a characteristic time is calculated, T_{micro}: the time taken for the mass flow rate to relax from a suddenly-applied pressure gradient to within 95% of its steady-state value.

5.3. Synthetic-jet operation

To achieve maximum flow response, the micro actuator of Fig. 14 is usually operated with a sinusoidal driver operating at, or near to, the Helmholtz frequency of the device (i.e., the frequency at which the plenum pressure would naturally oscillate, assuming flow in the slot acts inviscidly). Following analysis similar to that in [20], the Helmholtz frequency for this two-dimensional geometry is:

$$\omega_{\mathrm{H}} = \sqrt{\frac{WRT}{A_p L}}, \tag{40}$$

where A_p is the cross-sectional area of the plenum (see Fig. 14). For the simulations presented in this section, the volume changes generated by the motion of the diaphragm are modelled as a sinusoid at this Helmholtz frequency. The Helmholtz period thus represents a macro time scale ($T_{\mathrm{macro}} = 2\pi/\omega_H$) which allows the scale separation number to be expressed, using definition 1, as:

$$S = \frac{2\pi}{\omega_{\mathrm{H}} T_{\mathrm{micro}}}. \tag{41}$$

As mentioned at the end of Section 5.2, T_{micro} is the pressure-driven start-up time for the slot model in isolation.

For the first case (Case 1), we consider highly scale-separated conditions with moderate rarefaction in the slot: $S = 100$, $\mathrm{Kn} = 0.1$, $L/W = 10$. Fig. 15(a) and (b) show plots of mass-flow-rate and plenum-pressure evolution in the actuator, respectively, non-dimensionalised using appropriate combinations of external density ρ_{ext}, slot width W, and thermal speed $v = \sqrt{2RT}$. In this case, the external and initial plenum pressure are equal. The solid line in both these figures are the results

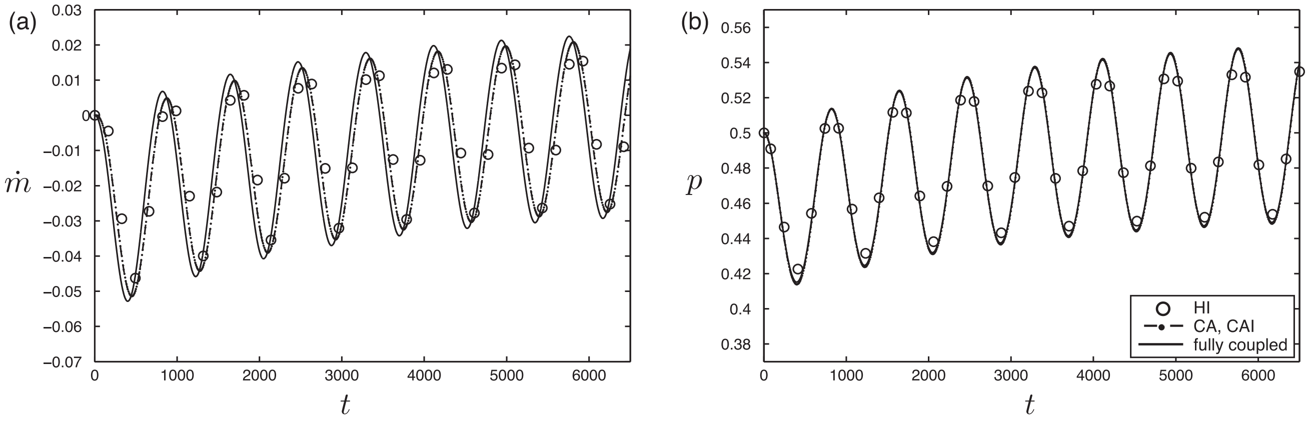

Fig. 15. Time-history plots of non-dimensional (a) mass flow rate and (b) plenum pressure. Comparison of fully-coupled (—), HI (∘), CA (– –) and CAI (···) solutions. Note, in all plots CA and CAI plots are indistinguishable and thus appear as (– · –). Case 1: $S = 100$, Kn = 0.1.

from a fully-coupled solution. A combination of the high scale separation and the intrinsic stiffness of the BGK numerics means that a very large number of time steps are required in the fully-coupled simulation: ∼1.3 million. Given that each micro time step is a two-dimensional calculation, this is not a trivial computation overall.

For the HI, CA and CAI schemes (also plotted in Fig. 15) the micro gearing is $g_{\text{micro}} = 20$. This means that there are 20× fewer BGK time steps performed in each of the methods, as compared to the fully-coupled solution. Other important parameters are: $n_{\text{macro}} = 100$ (chosen to sufficiently resolve macroscopic variations and maintain stability) and $r_{\text{stiff}} = 16$. The latter value, calculated from Eq. (3), is an indicator of the relative stiffness of the macro and micro models and affects the range of applicability of the time-stepping schemes, as summarised in Table 1. Of course, if the time-stepping of the BGK model were changed to an implicit scheme (as opposed to the explicit Lax–Wendroff) this stiffness would reduce considerably. However, high relative stiffness is probably more representative of a hybrid solver combining CFD with a molecular-based model (e.g. molecular dynamics).

The results in Fig. 15 indicate that all three methods agree quite closely with the fully-coupled simulation. Considering the computational speed up afforded by $g_{\text{micro}} = 20$, this is a considerable success. The CA and CAI schemes, although plotted separately in Fig. 15, are so close as to be indistinguishable. The major difference is the number of macro time-step operations performed in each: for the CA method ∼66,000, whereas for the CAI method only ∼800. The CAI method performs approximately 80× fewer macro time-step computations than the CA method to achieve, essentially, the same result.

Although in this example the macro computations are of negligible expense as compared to the BGK, this will not necessarily be the case for full-scale hybrid CFD/MD simulations, as argued in Section 2.1. The HI results in Fig. 15 are of reasonable accuracy but of poor resolution, because the requirement specified in Eq. (7) in Section 2.2 is not satisfied. In other words, to achieve the micro gearing (BGK speed-up) of 20, the HI method has had to sacrifice macro resolution (i.e. only 5 macro time steps are performed in one diaphragm period, as compared to 100 in the CAI method).

Figs. 16–18 show actuator results with modified case parameters. In Case 2 (Fig. 16) there is greater rarefaction (Kn = 1, $r_{\text{stiff}} = 9$); in Case 3 (Fig. 17) there is moderate scale separation ($S = 10$, $g_{\text{micro}} = 2$); in Case 4 (Fig. 18) there is little scale separation ($S = 1.5$, $g_{\text{micro}} = 1.1$); all other parameters, in each case, are the same as in Case 1. The HI results in Case 4 (Fig. 18) have such poor macro resolution and accuracy that the majority of points are not seen within the scales plotted.

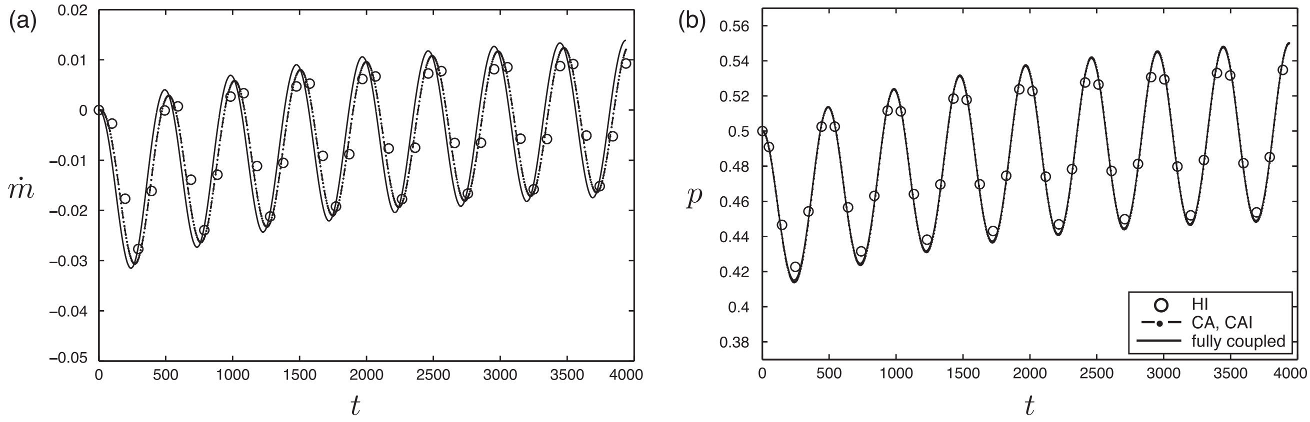

Fig. 16. Time-history plots of non-dimensional (a) mass flow rate and (b) plenum pressure. Comparison of fully-coupled (—), HI (∘), CA (– –) and CAI (···) solutions. Note, in all plots CA and CAI plots are indistinguishable and thus appear as (– · –). Case 2: $S = 100$, Kn = 1.

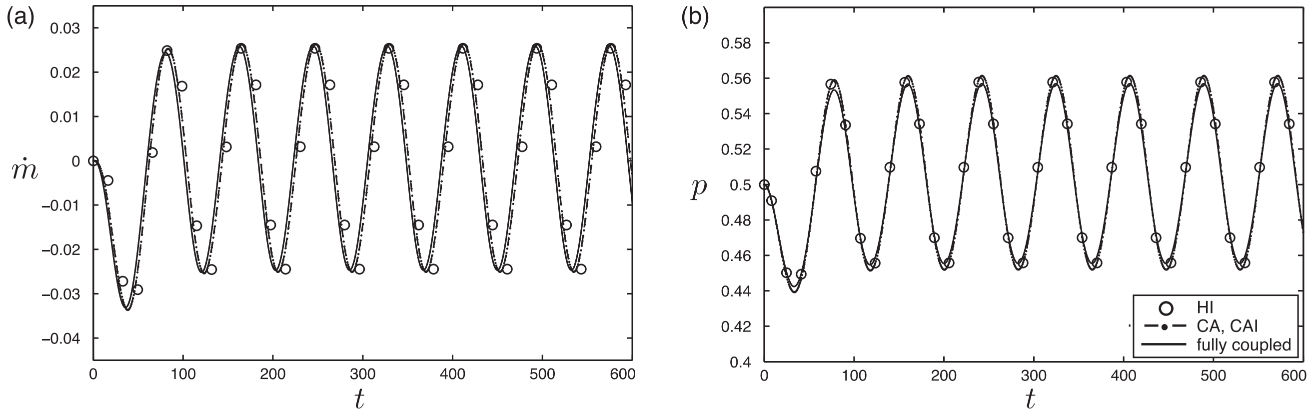

Fig. 17. Time-history plots of non-dimensional (a) mass flow rate and (b) plenum pressure. Comparison of fully-coupled (—), HI (○), CA (– –) and CAI (···) solutions. Note, in all plots CA and CAI plots are indistinguishable and thus appear as (– · –). Case 3: $S = 10$, Kn = 0.1.

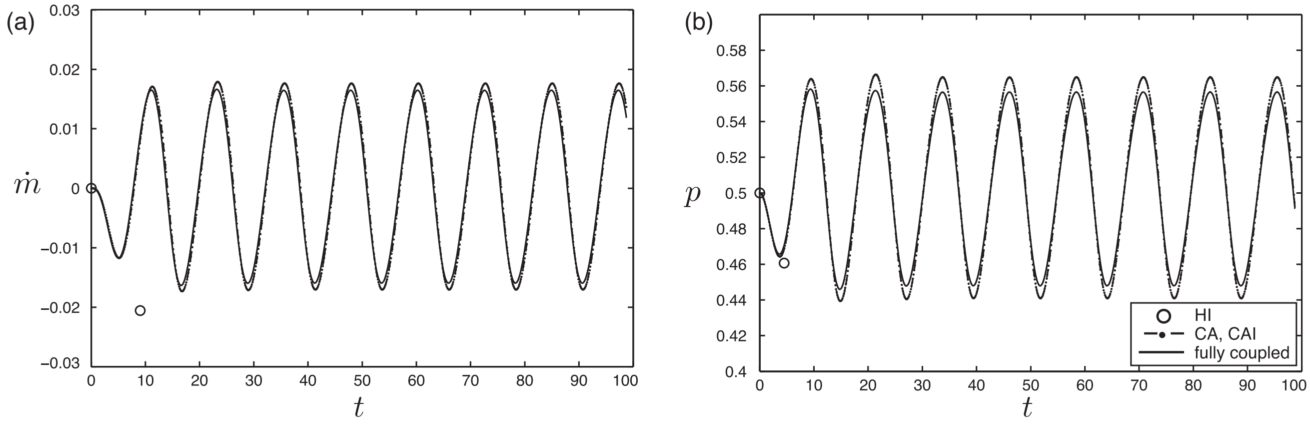

Fig. 18. Time-history plots of non-dimensional (a) mass flow rate and (b) plenum pressure. Comparison of fully-coupled (—), HI (○), CA (– –) and CAI (···) solutions. Note, in all plots CA and CAI plots are indistinguishable and thus appear as (– · –). Case 4: $S = 1.5$, Kn = 0.1.

These test cases show that the CAI and CA methods provide the same accurate prediction, but the CAI method requires far fewer macro time-step operations than the CA method (e.g., Case 2: ~50× fewer; Case 3: ~80× fewer; and Case 4: ~20× fewer).

5.4. Pressure-jump operation

In this section we investigate the response of the actuator to a step change in plenum pressure, as investigated in [13]. The initial plenum pressure is set 10% higher than the external pressure p_{ext}. Here, the time scale separation of the coupled system will vary with time, and so we use Eqs. (30) and (33) to evaluate the *local* scale separation and micro gearing, respectively. As discussed in Section 4, when using the local scale separation number, calculation of T_{macro} is replaced by a real-time measure of the temporal rates of change of the coupling variables (here, p and $\dot{m}$). So, in the evaluation of Eq. 33, $x = p, y = \dot{m}, p_{\text{ref}} = 0.1p_{\text{ext}}$ and $\dot{m}_{\text{ref}}$ is taken as the maximum expected value of the mass flow rate.[2] T_{micro} is calculated prior to the simulation as described at the end of Section 5.2. The proportionality constant relating the local scale separation to the micro gearing is chosen at a moderate value $k_g = 1/5$ (as used in the simulations presented in Fig. 13).

Plots of mass-flow-rate and plenum-pressure evolution in the actuator, after the initial jump in pressure, are presented in Figs. 19–21 for three different plenum sizes (here characterised by the Helmholtz frequency): Case 1 (Fig. 19) is for a large plenum (with, consequently, long macro time scales) $2\pi/(T_{\text{micro}}\omega_H) = 100$; Case 2 (Fig. 20) is a medium-sized plenum $2\pi/(T_{\text{micro}}\omega_H) = 10$; Case 3 (Fig. 21) is a small plenum $2\pi/(T_{\text{micro}}\omega_H) = 1$. For each case Kn = 0.1, $r_{\text{stiff}} = 82$ and all else is the same as that described in Section 5.3.

The conclusions that can be drawn from these results are similar to those drawn from the results in Section 5.3. First, the HI scheme does not have sufficient macroscopic resolution and, as a result, the error is unacceptably high (particularly for Case 3). It is therefore discounted from our considerations of efficiency. Second, the CAI and CA provide an equally accurate

---

[2] For consistency, here we took this value from a fully-coupled simulation, but in practice this would need to be estimated.

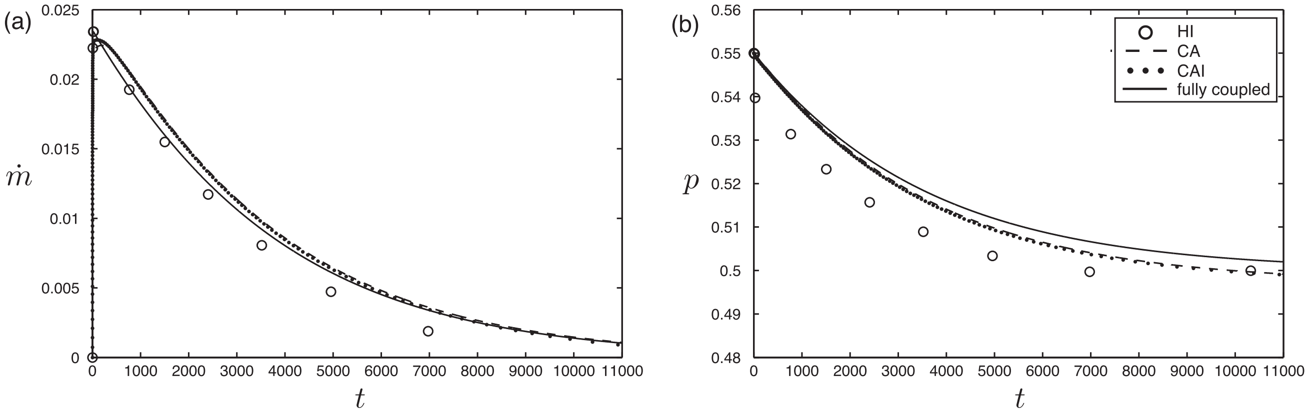

Fig. 19. Time-history plots of non-dimensional (a) mass flow rate and (b) plenum pressure. Comparison of fully-coupled (—), HI (∘), CA (– –) and CAI (···) solutions. Case 1: $2\pi/(T_{\text{micro}}\omega_H)$=100.

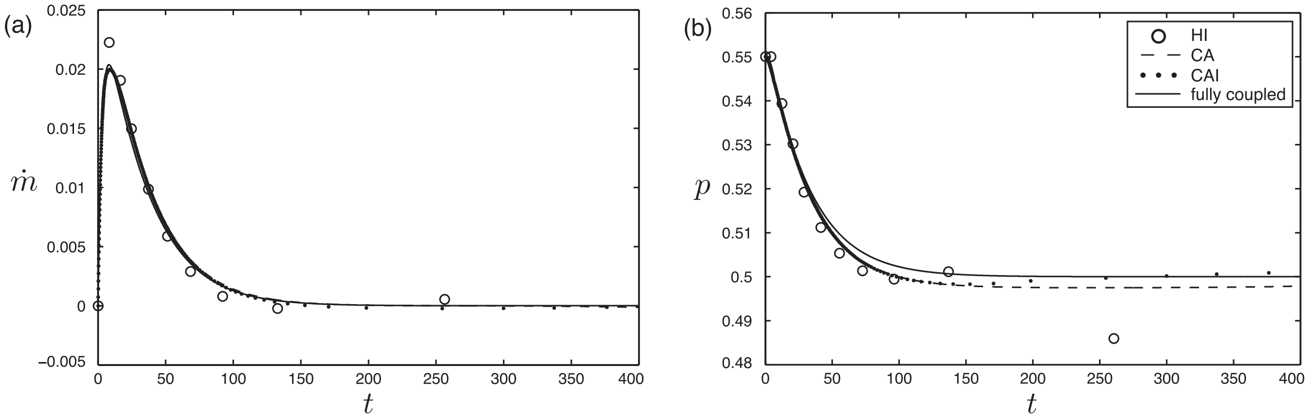

Fig. 20. Time-history plots of non-dimensional (a) mass flow rate and (b) plenum pressure. Comparison of fully-coupled (—), HI (∘), CA (– –) and CAI (···) solutions. Case 2: $2\pi/(T_{\text{micro}}\omega_H)$ = 10.

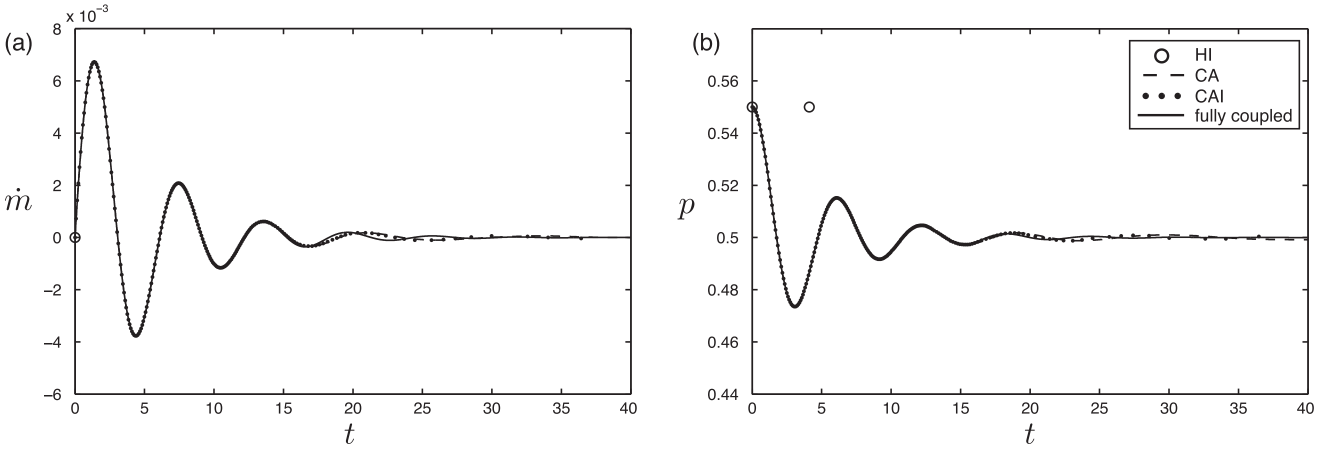

Fig. 21. Time-history plots of non-dimensional (a) mass flow rate and (b) plenum pressure. Comparison of fully-coupled (—), HI (∘), CA (– –) and CAI (···) solutions. Case 3: $2\pi/(T_{\text{micro}}\omega_H)$ = 1.

result (as compared to a fully-coupled solution) while reducing the total number of micro (BGK) time steps calculated: for Case 1, ∼200× fewer; for Case 2, ∼10× fewer; and for Case 3, ∼2× fewer. In terms of macro time steps, though, the CAI is far more efficient: for Case 1 the CAI calculates ∼270× fewer macro time steps than the CA method; for Case 2, ∼210× fewer; and for Case 3, 110× fewer.

Table 3
Number of macro and micro time-step operations performed for simulations presented in Figs. 19–21 (Cases 1–3) for the fully-coupled, CA and CAI schemes.

	Fully-coupled (macro/micro)	CA (macro/micro)	CAI (macro/micro)
Case 1	11M/11M	51k/51k	190/54k
Case 2	410k/410k	38k/38k	190/42k
Case 3	41k/41k	23k/23k	210/23k

Table 3 summarise the total number of macro and micro time-step operations performed for Cases 1–3 for the fully-coupled, CA and CAI schemes.

6. Example III: a micro-gas journal bearing

In this final example, the transient response of a micro gas bearing is modelled; the plain bearing is illustrated schematically in Fig. 22. Key features of the configuration are that the width of the bearing gap W is of comparable magnitude to the mean-free path (specifically, $\mathrm{Kn} = \lambda/W = 0.1$), and that this in turn is much smaller than the central shaft radius, r (i.e., $r \gg W$). We consider the transient response of a stationary shaft and gas layer to the sudden application of a shaft torque per unit length, T_{A}.

In contrast to the previous example (Section 5) in this problem it is not possible to sub-divide the flow within the gas annulus into a region requiring a gas-kinetic treatment and a region that does not: strictly speaking, because the Knudsen number is relatively high, the entire annulus requires solution using a gas-kinetic model. A pragmatic solution to this problem is to note that $W \ll r$, allowing us to represent the annulus with a 1D Couette-flow simulation (as depicted in Fig. 22). This approach has more in common with HMM [2] than domain decomposition.

6.1. Governing equations

A macro equation governing the evolution of the tangential velocity of the shaft at the periphery, v_{wall}, is obtainable directly from Newton's second law:

$$\frac{\mathrm{d}v_{\mathrm{wall}}}{\mathrm{d}t} = \frac{r}{I}(T_{\mathrm{A}} - 2\pi r \tau_{\mathrm{wall}}), \tag{42}$$

where τ_{wall} is the shear stress acting on the shaft (generated in the gas layer), which is calculated by the 1D micro model. The moment of inertia per unit length of the shaft I can be expressed in terms of the initial acceleration of the shaft and the applied torque:

$$I = rT_{\mathrm{A}}\left(\left.\frac{\mathrm{d}v_{\mathrm{wall}}}{\mathrm{d}t}\right|_{t=0}\right)^{-1}. \tag{43}$$

Eq. (42) is solved using an implicit second-order Euler scheme, the same as for the macro equations of Sections 4 and 5. The micro model for the rarefied gas layer (represented as a parallel Couette flow) is again the BGK-Boltzmann Eq. (38). All computational details for the BGK solution are the same as for our pressure-jump simulations in Section 5.4, except that T_{micro} is

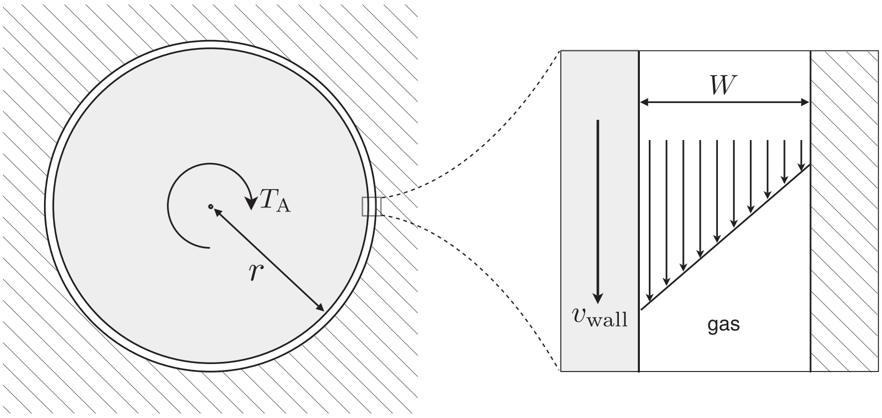

Fig. 22. Schematic of a micro gas bearing.

based on relaxation of the mass flow rate to a suddenly-applied wall velocity (as opposed to a pressure gradient). Since the time scale separation will vary with time, we use Eq. (33) to evaluate the local scale separation with $x = v_{\text{wall}},\ y = \tau_{\text{wall}}$, and with reference values taken from the steady state (pre-calculation of T_{macro} is therefore not needed). The wall velocity v_{wall} is a coupling variable passed to the BGK (micro) solver from the macro solution of (42). The wall shear stress is obtained from the micro model by taking the appropriate second moment of the distribution function.

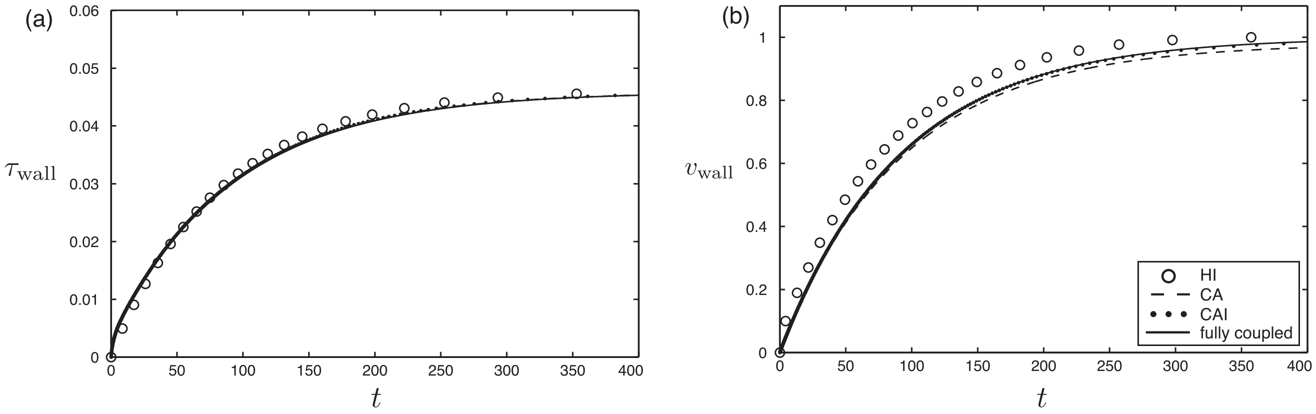

Fig. 23. Time-history plots of non-dimensional (a) wall shear stress and (b) bearing wall velocity. Comparison of fully-coupled (—), HI (○), CA (– –) and CAI (···) solutions. Case 1: $(\mathrm{d}v_{\text{wall}}/\mathrm{d}t)_{t=0} = v_{\text{steady}}/(5T_{\text{micro}})$.

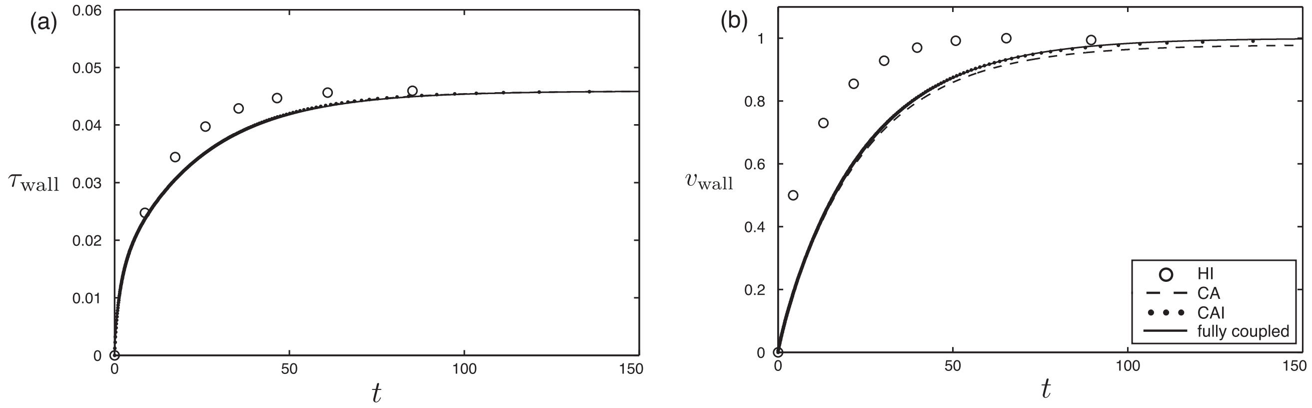

Fig. 24. Time-history plots of non-dimensional (a) wall shear stress and (b) bearing wall velocity. Comparison of fully-coupled (—), HI (○), CA (– –) and CAI (···) solutions. Case 2: $(\mathrm{d}v_{\text{wall}}/\mathrm{d}t)_{t=0} = v_{\text{steady}}/T_{\text{micro}}$.

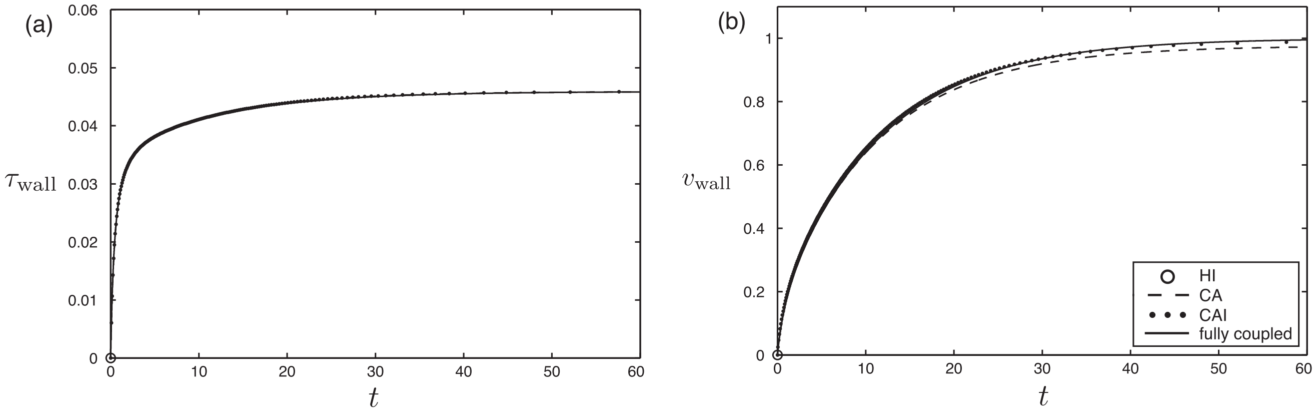

Fig. 25. Time-history plots of non-dimensional (a) wall shear stress and (b) bearing wall velocity. Comparison of fully-coupled (—), HI (○), CA (– –) and CAI (···) solutions. Case 3: $(\mathrm{d}v_{\text{wall}}/\mathrm{d}t)_{t=0} = 5v_{\text{steady}}/T_{\text{micro}}$.

Table 4
Number of macro and micro time-step operations performed for simulations presented in Figs. 23–25 (Cases 1–3) for the fully-coupled, CA and CAI schemes.

	Fully-coupled (macro/micro)	CA (macro/micro)	CAI (macro/micro)
Case 1	400k/400k	146k/146k	320/150k
Case 2	150k/150k	67k/67k	224/71k
Case 3	60k/60k	37k/37k	186/40k

Figs. 23–25 show plots of the transient step response of the shear stress and bearing velocity v_{wall} to the suddenly applied torque. Three cases are considered with different initial accelerations: Case 1, $(\mathrm{d}v_{\text{wall}}/\mathrm{d}t)_{t=0} = v_{\text{steady}}/(5T_{\text{micro}})$, Fig. 23; Case 2, $(\mathrm{d}v_{\text{wall}}/\mathrm{d}t)_{t=0} = v_{\text{steady}}/T_{\text{micro}}$, Fig. 24; and Case 3 $(\mathrm{d}v_{\text{wall}}/\mathrm{d}t)_{t=0} = 5v_{\text{steady}}/T_{\text{micro}}$, Fig. 25; where v_{steady} is the steady-state velocity of the shaft's peripheral wall. The applied torque T_A is chosen in each case such that $v_{\text{steady}} = 1$ (the non-dimensionalisation is as in Section 5). Results from the three schemes (HI, CA, and CAI) are compared to the fully-coupled solution (solid lines in Figs. 23–25). For these simulations: $k_g = 1/5$, $n_{\text{macro}} = 100$ and $r_{\text{stiff}} = 86$.

It is again clear that the accuracy and stability of the HI method is severely compromised when the problem exhibits any non-scale-separated periods. For example, in Case 3 where the macro time scales are short, the HI results can only be seen on Fig. 25 at time zero. Our conclusions in the previous sections are also reinforced by the performance of the CA and CAI schemes. Both provide good accuracy, as compared to the fully-coupled solution, for all cases, but with fewer micro (BGK) time step operations. CAI has the advantage, overall, since it requires far fewer macro time-step operations than the CA scheme. Table 4 summarises the macro and micro time step operations used in each of the three cases for the fully-coupled, CA and CAI schemes.

7. Summary and Conclusions

In this paper a new method has been proposed for exploiting time-scale separation in hybrid simulations of multiscale flows. The scheme is, in some senses, a generalisation of the time-stepping proposed in HMM [1] (referred to in this paper as the HI method) and the time-stepping in seamless HMM [6] (referred to in this paper as the CA method), combining the desirable features of both. The CAI scheme we propose, illustrated in Fig. 1(e), is equivalent to the CA method, unless the macro time step becomes smaller than it needs to be to guarantee an adequate (and pre-defined) macro resolution, in which case the number of time steps per coupling instance is increased (making it more like the HI method). This inherent adaptability gives the CAI scheme the range of applicability of the CA method, while maintaining the macro-time-step efficiency of the HI method as much as possible.

The three methods capable of reducing micro time-step operations (the HI, CA, and our CAI scheme) have been applied to three different application examples. Each scheme is implemented, numerically, using a leapfrog advancement, which we also propose as an improvement, in terms of numerical accuracy, to the standard simultaneous approach. In all the cases we considered, the CAI scheme performs as well as, or much better than the other schemes, in terms of both overall accuracy and efficiency. The scheme we propose combines the best of the respective methods with little additional complexity.

Future work will include the application of this scheme to CFD/molecular-dynamics hybrid models, where the impact of statistical noise from the molecular dynamics simulation on the CFD will need to be assessed.

Acknowledgments

This research is financially supported by EPSRC Programme Grant EP/I011927/1. The authors thank Prof Dimitris Valougeorgis for providing a well-documented DVM code that helped to generate the BGK results presented in this paper. The authors would also like to thank the reviewers of this paper for their helpful comments.

References

[1] W.Q. Ren, E. Weinan, Heterogeneous multiscale method for the modeling of complex fluids and micro-fluidics, J. Comput. Phys. 204 (2005) 1–26.
[2] W. E, B. Engquist, X.T. Li, W.Q. Ren, E. Vanden-Eijnden, Heterogeneous multiscale methods: a review, Commun. Comput. Phys. 2 (2007) 367–450.
[3] M. Kalweit, D. Drikakis, Multiscale simulation strategies and mesoscale modelling of gas and liquid flows, IMA J. App. Math. 76 (2011).
[4] R. Delgado-Buscalioni, P.V. Coveney, Hybrid molecular-continuum fluid dynamics, Phil. Trans. Roy. Soc. A – Math. Phys. Eng. Sci. 362 (2004) 1639–1654.
[5] K.M. Mohamed, A.A. Mohamad, A review of the development of hybrid atomistic-continuum methods for dense fluids, Microfluid. Nanofluid. 8 (2010) 283–302.
[6] W. E, W.Q. Ren, E. Vanden-Eijnden, A general strategy for designing seamless multiscale methods, J. Comput. Phys. 228 (2009) 5437–5453.
[7] M. Gad-el Hak, The fluid mechanics of microdevices – the freeman scholar lecture, J. Fluids Eng. 121 (1999) 5–33.
[8] D.A. Lockerby, J.M. Reese, H. Struchtrup, Switching criteria for hybrid rarefied gas flow solvers, Proc. Roy. Soc A – Math. Phys. Eng. Sci. 465 (2009) 1581–1598.
[9] L.N. Cattafesta, M. Sheplak, Actuators for active flow control, Ann. Rev. Fluid Mech. 43 (2011) 247–272.
[10] A. Glezer, M. Amitay, Synthetic jets, Ann. Rev. Fluid Mech. 34 (2002) 503–529.
[11] R.R. Rathnasingham, K.S. Breuer, Coupled fluid-structural characteristics of actuators for flow control, AIAA J. 35 (1997) 832–837.
[12] D.A. Lockerby, P.W. Carpenter, C. Davies, Control of sublayer streaks using microjet actuators, AIAA J. 43 (2005) 1878–1886.
[13] D.A. Lockerby, P.W. Carpenter, Modeling and design of microjet actuators, AIAA J. 42 (2004) 220–227.

[14] D.A. Lockerby, P.W. Carpenter, C. Davies, Is Helmholtz resonance a problem for micro-jet actuators?, Flow Turbul Combust. 78 (2007) 205–222.
[15] M. Chaudhari, B. Puranik, A. Agrawal, Multiple orifice synthetic jet for improvement in impingement heat transfer, Int. J. Heat Mass Transfer 54 (2011) 2056–2065.
[16] Cercignani, Mathematical Methods in Kinetic Theory, Springer, 1990.
[17] S. Naris, D. Valougeorgis, The driven cavity flow over the whole range of the Knudsen number, Phys. Fluids 17 (2005).
[18] D. Valougeorgis, Couette-flow of a binary gas-mixture, Phys. Fluids 31 (1988) 521–524.
[19] D. Valougeorgis, S. Naris, Acceleration schemes of the discrete velocity method: gaseous flows in rectangular microchannels, SIAM J. Sci. Comput. 25 (2003) 534–552.
[20] A. Dowling, J. Ffowcs Williams, Sound and Sources of Sound, Horwood, Chichester, England, 1983.